Nano Research Energy

ISSN 2791-0091 (print); 2790-8119 (online)
https://doi.org/10.26599/NRE.2026.9120236

Review Article

Atomic-scale interface engineering in photocatalysis

Haiqing Wang (✉)

Shandong Key Laboratory of Functional Materials for Integrated Lithium Niobate Photonics, Institute of Advanced Interdisciplinary Research (IAIR), College of Chemistry and Chemical Engineering, University of Jinan, Jinan 250022, China

Received: 31 March 2026 / **Revised:** 22 April 2026 / **Accepted:** 5 May 2026 / **Published date:** 5 June 2026

ABSTRACT

Interfaces are central to photocatalytic solar-to-chemical conversion. Conventional heterointerfaces mainly optimize band alignment and macroscopic charge separation. Atomic-scale interface engineering in photocatalysis denotes the strategic construction of atomically precise interfacial architectures with controlled chemical bonding, lattice coherence, and coordination environments, thereby governing interfacial charge redistribution, carrier routing, and reaction intermediate activation at atom level. In this review, we highlight advanced synthetic approaches-including seed-mediated growth, cation exchange, and coordination-confined anchoring-and discuss how *operando* spectroscopy combined with density functional theory elucidates interfacial electric fields and orbital coupling in steering multi-electron reactions such as CO_2 reduction and H_2 evolution. We further systematically summarize the design principles and the recent development of covalently bridged ensembles, epitaxial heterointerfaces, defect-mediated boundaries, and atomically dispersed single/dual-atom sites. Finally, emerging directions in superlattice engineering and dipole-induced polarization are outlined to guide the rational development of next-generation photocatalysts with enhanced quantum efficiency and product selectivity.

KEYWORDS

atomic-scale interface, orbital coupling, interfacial electric field, CO_2 reduction, H_2 evolution

1 Introduction

Interfaces play a pivotal role in heterostructured photocatalysts [1, 2]. Although photon absorption primarily occurred within the bulk semiconductor, charge separation, carrier extraction, and surface redox reactions proceeded at interfacial boundaries [3]. The establishment of interfacial electric fields, band bending, and atomic-level orbital hybridization dictated carrier dynamics and reaction energetics [4–6]. In this sense, photocatalysis functioned fundamentally as an interface-controlled process rather than a purely bulk-driven event [7]. Conventional heterointerfaces mainly regulated band alignment and macroscopic charge separation [8]. However, they lacked atomic precision in defining bonding configurations, coordination environments, and adsorption geometries, which limited their ability to rationally control reaction pathways.

Against this background, atomic-scale interface engineering emerged as a more deterministic strategy [9, 10]. It denoted the strategic construction of atomically precise interfacial architectures with controlled chemical bonding, lattice coherence, and coordination environments, thereby governing interfacial charge redistribution, carrier routing, and reaction intermediate activation at the atomic level [11–13]. Atomic-scale interfaces in photocatalytic systems were broadly classified into several representative categories. Atomic-scale interfaces discussed in this Review were categorized into five types [14–20]: (i) epitaxial interface engineering, where lattice matching and oriented growth created coherent junctions; (ii) interfacial chemical bridges engineering, in which directional bonds (e.g., M-O-M', M-S, M-P-N) were established; (iii) organic-inorganic bonded interfaces engineering, leveraging covalent/coordination/hydrogen-bond links to couple molecular orbitals with semiconductors; (iv) dual-atom type interfaces engineering; and (v) A-B-A-B copolymer-analogue interfaces engineering, featuring periodic stacking/dipole superposition. Detailed mechanisms and representative examples are presented in Section 4.

Based on extensive reports on photocatalytic H_2 production and CO_2 reduction, atomic-scale interface engineering offered several decisive advantages in photocatalysis in contrast to conventional interfaces: (i) it enabled precise control over interfacial bonding configurations, coordination environments, and lattice coherence, thereby creating predictable orbital hybridization and localized charge redistribution at specific atomic sites [20]; (ii) it promoted directional carrier migration through built-in electric fields and atomically defined charge-transfer pathways, which effectively suppressed recombination and improved charge utilization efficiency [21]; (iii) it tailored the adsorption geometries, binding strengths, and activation modes of

Address correspondence to Haiqing Wang, ifc_wanghq@ujn.edu.cn

key intermediates, thus lowering reaction barriers and steering product selectivity [22, 23]; (iv) it facilitated cooperative multi-site catalysis, especially in multi-electron reactions such as H_2 evolution and CO_2 reduction, by stabilizing crucial intermediates and enhancing coupling steps [24]; and (v) it provided a rational structure-property framework that linked atomic arrangement with electronic structure, carrier dynamics, and catalytic performance, offering a more deterministic route for designing highly efficient, selective, and stable photocatalytic systems [17]. Such insights provide fundamental principles for rational catalyst design and facilitate the development of highly efficient solar-to-chemical conversion systems. Therefore, a comprehensive review of atomic-scale interface engineering in photocatalysis is of critical importance for guiding future research and advancing the field.

In this review, we underscore the pivotal significance of atomic-scale interface engineering to simultaneously regulate charge redistribution, reaction pathway, and intermediate stabilization in photocatalytic solar-to-chemical conversion (Scheme 1). The construction strategies were first outlined, including seed-mediated growth, epitaxial growth, ion-exchange-enabled upgrading, and coordination-confined anchoring. On this basis, we systematically summarize representative interface archetypes, such as highly matched epitaxial interfaces, chemical bond-bridged interface, organic-inorganic bonded interface, dual-atom motifs, and A-B-A-B copolymer-analogue structure. A systematic framework that links lattice registry, interfacial chemical bridges, and local polarization with built-in electric fields, orbital coupling, and multi-electron reaction energetics was established for photocatalytic H_2 evolution and CO_2 reduction. Finally, we discuss the remaining challenges and emerging opportunities in atomic-scale interface engineering to guide the rational design of next-generation photocatalysts with improved quantum efficiency, selectivity, and stability.

2 Mechanisms of photocatalytic H_2 evolution and CO_2 reduction

Photocatalytic H_2 production from water splitting begins with the absorption of photons by a semiconductor catalyst (Fig. 1) [26–28]. When the catalyst is irradiated with light whose energy

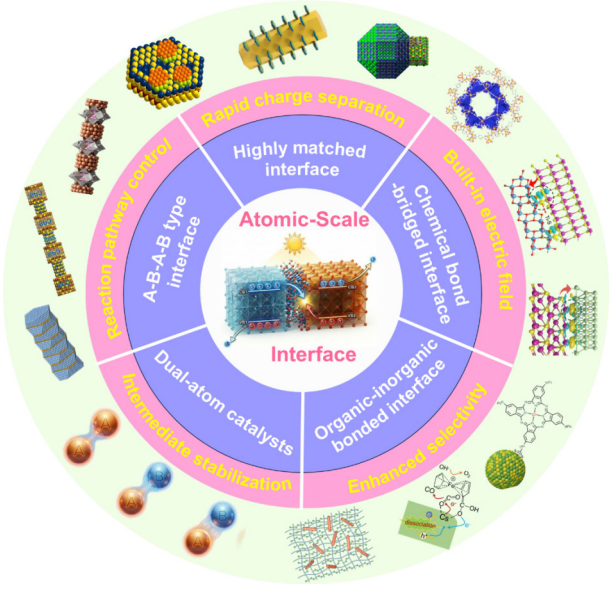

Scheme 1 Schematic illustration of engineering atomic-scale interfaces for photocatalytic H_2 evolution and CO_2 reduction.

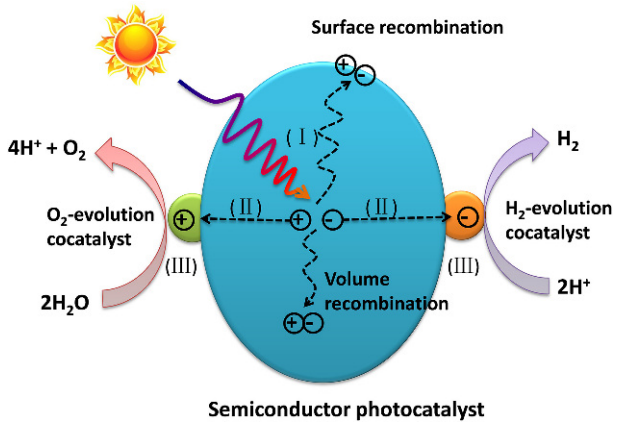

Figure 1 Schematic illustration of the process of photocatalytic H_2 evolution using semiconductor-based materials. Reprinted with permission from Ref. [25], © 2021 John Wiley & Sons Ltd.

exceeds its band gap, electrons in the valence band are excited to the conduction band, leaving holes in the valence band and forming electron-hole pairs. A fraction of these photogenerated carriers rapidly recombine, while the remaining electrons and holes separate and migrate through the bulk toward the catalyst surface [11]. Effective photocatalysis requires that this charge separation and migration occur faster than recombination. Once reaching the surface, conduction-band electrons participate in the hydrogen evolution reaction by reducing protons to generate H_2, whereas the valence-band holes oxidize water or sacrificial agents. The efficiency of this process strongly depends on light absorption capability, carrier separation efficiency, and interfacial reaction kinetics. To improve these steps, cocatalysts are often introduced onto semiconductor surfaces [25, 29]. Suitable cocatalysts can provide active sites for hydrogen evolution, reduce the activation barrier of surface reactions, and facilitate directional electron transfer [30]. By forming heterostructures with semiconductors, these cocatalysts promote charge separation and accelerate surface redox reactions (Fig. 1), thereby enhancing overall photocatalytic hydrogen production efficiency.

Several representative configurations have been developed to drive heterogeneous photocatalytic CO_2 reduction (Fig. 2(a)) [31]. One common system uses a single semiconductor catalyst combined with an external cocatalyst, which can be either conventional nanoparticles or isolated single-atom sites to accelerate surface reactions. Another approach relies on type-II heterostructures, where two semiconductors with staggered band structures promote spatial separation of photogenerated electrons and holes. In addition, Z-scheme photocatalysts were designed to maintain strong redox potentials while enabling efficient carrier transfer between two components [32]. Plasmonic metal-based systems constitute another category, in which localized surface plasmon resonance (LSPR) enhances light harvesting and generates energetic electrons for CO_2 activation. Finally, photosensitizer-catalyst coupled systems employ light-absorbing molecules to capture visible light and transfer excited electrons to catalytic centers for reduction reactions. Together, these configurations represent major strategies for improving light utilization, charge dynamics, and catalytic activity in photocatalytic CO_2 conversion [33].

By outlining the fundamental pathways of CO_2 photoreduction (Fig. 2(b)), we aimed to illustrate how rational interface engineering can regulate key elementary steps such as charge separation, interfacial electron transfer, CO_2 adsorption/activation,

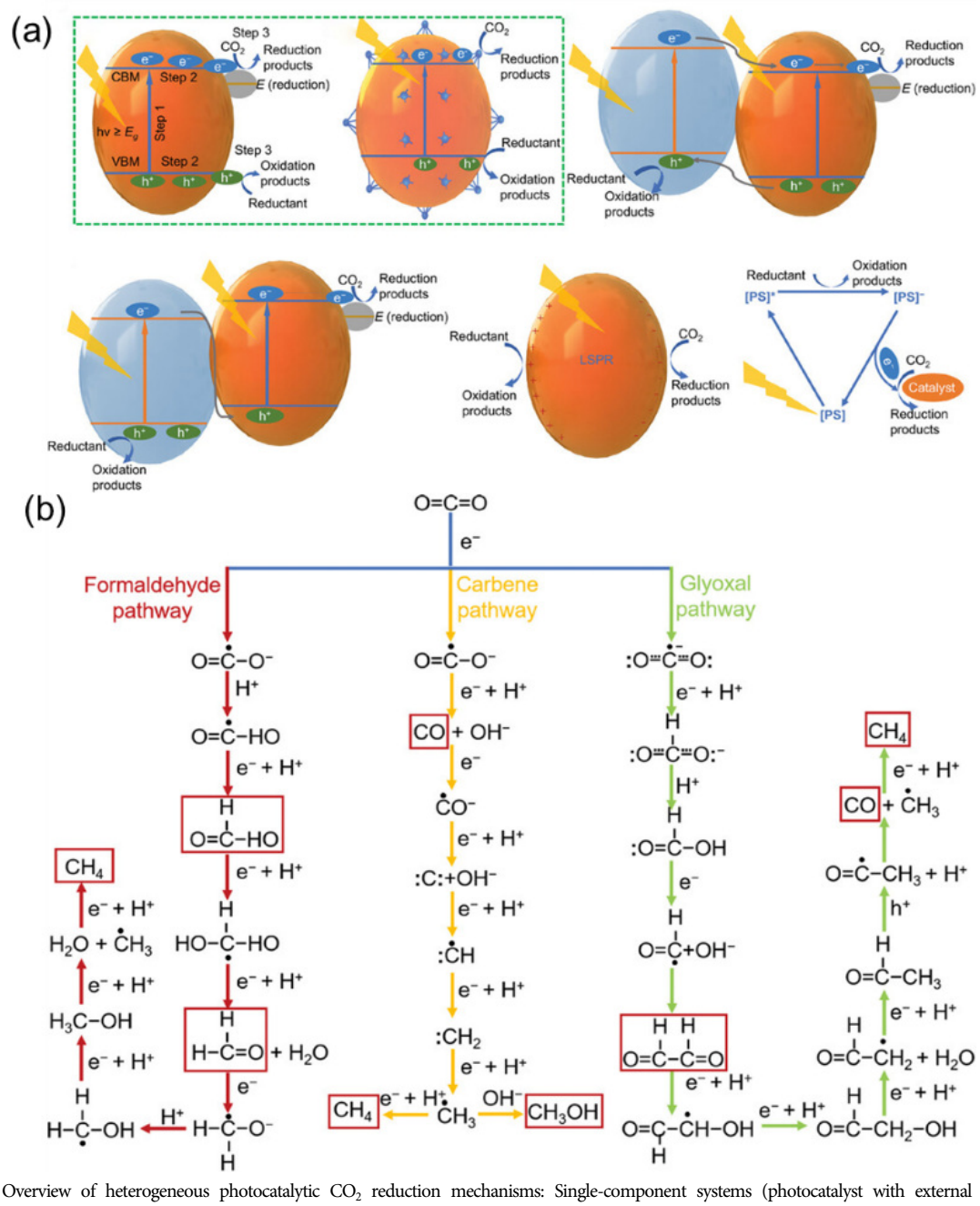

Figure 2 (a) Overview of heterogeneous photocatalytic CO_2 reduction mechanisms: Single-component systems (photocatalyst with external or single-atom cocatalyst), Heterojunction systems (Type-II heterostructure and Z/S-scheme), and Hybrid systems (LSPR-mediated metal photocatalyst and photosensitizer-catalyst assembly). Reprinted with permission from Ref. [31], © 2024 Jia, G. R. et al. Published by American Chemical Society. (b) Photocatalytic CO_2 reduction pathways (Released molecules are marked with red frames). Reprinted with permission from Ref. [32], © 2022 Wang, Y. O. et al. Published by American Chemical Society.

intermediate stabilization, and C-C coupling processes. Photocatalytic CO_2 reduction begins with the efficient charge separation and transport. When the catalyst is illuminated with photons whose energy exceeds its band gap. At the surface, photogenerated electrons reduce adsorbed CO_2 molecules through a sequence of proton-coupled electron transfer steps, forming intermediates such as $*CO_2^-$, *COOH, and *CO [17]. These intermediates can further undergo hydrogenation or coupling reactions to produce value-added products including CO, CH_4, CH_3OH, or other hydrocarbons. Meanwhile, the photogenerated holes oxidize water or sacrificial donors to supply protons and maintain charge balance. Because CO_2 is a highly stable linear molecule, its activation requires multiple electrons and protons, and most reduction steps occur through coupled proton-electron transfer processes. Depending on the reaction pathway, different products require different numbers of electrons and protons [34]. For example, the formation of CO follows a two-electron and two-proton process, whereas deeper reduction to CH_4 requires eight electrons and eight protons. Mechanistically, three typical pathways have been proposed (Fig. 2(b)) [32]. The first is the *COOH pathway, where CO_2 is first protonated to form a carboxyl intermediate (*COOH) and then reduced to CO. The second is the *OCHO pathway, in which CO_2 binds through oxygen to produce a formate intermediate (*OCHO), leading mainly to formate or formic acid. The third route involves further hydrogenation of the *CO intermediate to generate more reduced products such as CH_4 or CH_3OH. The key difference among these pathways lies in the initial adsorption configuration and the

stabilization of intermediates, which determines product selectivity and reaction energetics. Designing catalysts that regulate electron transfer and stabilize specific intermediates is therefore essential for efficient photocatalytic CO_2 conversion.

Multicarbon products (C_{2+}) are particularly valuable in photocatalytic CO_2 reduction because they possess higher energy density, greater economic value, and broader applicability as fuels and chemical feedstocks compared with C_1 products [35, 36]. Photocatalytic reduction of CO_2 to multicarbon products involves a complex sequence of proton-coupled electron transfer and C-C coupling steps on catalytic surfaces. Compared with C_1 products, the formation of C_{2+} species requires a much larger number of electrons and protons and therefore proceeds through deeper hydrogenation pathways. For example, the formation of C_2H_4 generally involves about 12 electrons and 12 protons, while C_2H_5OH requires a similar multi-electron and multi-proton transfer process [37–39]. Mechanistically, CO_2 is first activated to form key intermediates such as *COOH or *CO through a two-electron proton-coupled step. The generated *CO species then accumulate on adjacent catalytic sites and undergo C-C coupling to produce intermediates such as *OCCO or *CO-CO [40, 41]. Subsequent hydrogenation and protonation steps gradually convert these intermediates into more reduced multicarbon products, including ethylene, ethanol, or other C_{2+} hydrocarbons. The efficiency of this process strongly depends on the ability of the catalyst to stabilize *CO intermediates, promote their surface coupling, and maintain efficient electron and proton supply [2, 42]. Therefore, catalyst designs that provide neighboring active sites, facilitate charge transfer, and regulate intermediate adsorption are essential for efficient photocatalytic formation of multicarbon products.

Photocatalytic CO_2 reduction and H_2 evolution both involve complex processes of light absorption, charge separation, and surface redox reactions, yet their efficiencies are often limited by sluggish carrier transfer and poorly defined reaction sites. Atomic-scale interface engineering provides an effective strategy to address these challenges by precisely controlling interfacial bonding configurations, coordination environments, and electronic structures. Such atomically defined interfaces can promote directional charge migration, create strong built-in electric fields, and tailor the adsorption and activation of key intermediates. As a result, they simultaneously accelerate proton reduction for H_2 evolution and facilitate the multi-electron reduction of CO_2. Therefore, constructing well-defined atomic-scale interfaces is crucial for improving catalytic efficiency, reaction selectivity, and overall solar-to-chemical energy conversion in photocatalytic systems.

3 Construction of atomic-scale interfaces

3.1 Seed-mediated growth

Seed-mediated growth played a pivotal role in constructing well-defined heterogeneous interfaces. Seed-mediated growth was generally understood as a kinetically regulated heterogeneous nucleation process in which preformed crystalline seeds directed subsequent deposition of secondary components. Three growth modes of Frank-van der Merwe (FM, layer-by-layer), Stranski-Krastanov (SK, layer-plus-island), and Volmer-Weber (VW, island) (Fig. 3(a)) [43, 44]. The FM mode occurred in systems with minimal lattice mismatch (<2%), where the deposited atoms favored bonding with the substrate, resulting in smooth and layer-by-layer growth [45]. Conversely, the VW mechanism dominated highly mismatched systems (>10%). The adatom-adatom interactions surpassed substrate bonding, leading to the direct nucleation of 3D islands without an initial wetting layer favoring to relieve strain. The SK mode represented an intermediate pathway at moderate mismatch (2%–10%). The initial 2D layers were formed, but subsequently transitioned into 3D clusters once the accumulated elastic strain reached a critical threshold [46, 47]. Taken together, the FM growth ensured structural uniformity for multi-layered coatings. The VW and SK modes offered essential routes for creating high-surface-area nanostructures. The three modes provide researchers with versatile strategies to tailor the electronic and catalytic properties of diverse nanomaterials [44]. When the lattice parameters or crystal symmetry of the seed and the grown component are not well matched, strain can develop at the interface during growth. This may generate dislocations, vacancies, dangling bonds, or partially incoherent boundaries. Such defects often serve as charge recombination centers, hinder carrier transport, weaken interfacial electronic coupling, and reduce structural stability, which can lower photocatalytic performance. At the same time, defects are not always harmful. The moderate amount of defects can create active sites, adjust the band structure, and promote reactant adsorption. Therefore, the key challenge is to properly control lattice mismatch and defect density to obtain beneficial interface properties.

In most reports, the mechanism relied on lowering the interfacial energy barrier and confining nucleation onto specific crystallographic facets, thereby suppressing homogeneous nucleation in solution [48, 49]. Such a pathway enabled

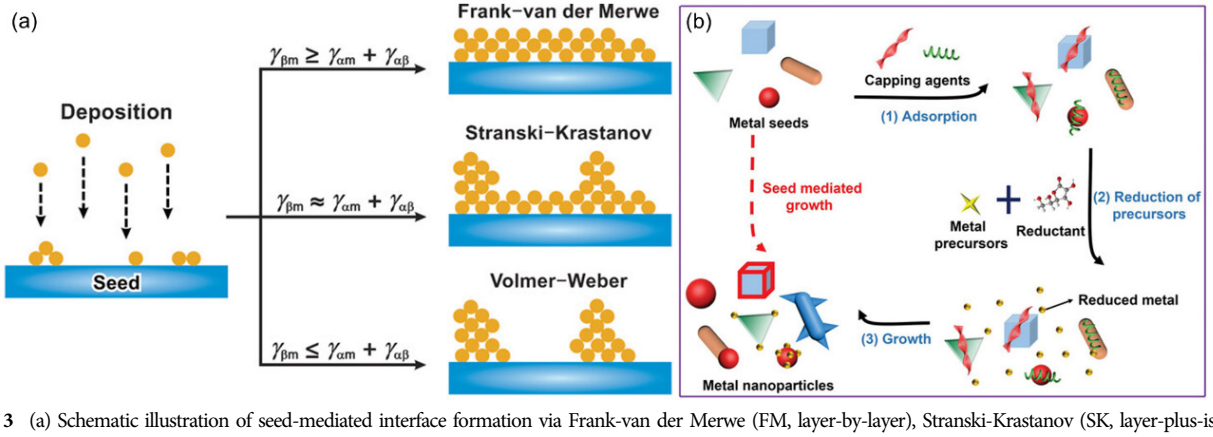

Figure 3 (a) Schematic illustration of seed-mediated interface formation via Frank-van der Merwe (FM, layer-by-layer), Stranski-Krastanov (SK, layer-plus-island), and Volmer-Weber (VW, island) modes. Reprinted with permission from Ref. [43], © 2017 Wiley-VCH Verlag GmbH & Co. KGaA, Weinheim. (b) Typical implementation pathways of seed-mediated interface formation. Reprinted with permission from Ref. [44] , © 2023 Wiley-VCH GmbH.

anisotropic growth, facet-selective overgrowth, and strain-modulated branching, which were extensively demonstrated in noble metal systems to tailor plasmonic and photothermal properties (Fig. 3(b)) [50]. The structural features generated by this strategy typically included core-shell, core-satellite, yolk-shell, and branched architectures, where lattice matching, surface ligand coordination, and precursor reduction kinetics collectively determined shell continuity and epitaxial coherence [51, 52]. Importantly, this mechanism was not restricted to metallic crystals. In semiconductor nanocrystals, seeded-mediated growth was successfully employed to fabricate type-I and type-II core-shell quantum dots, where controlled shell deposition passivated surface traps and engineered band alignment for directional charge separation [53]. For example, CdSe/CdS [54] and Cu_2S/CdS [55] heterostructures were constructed through stepwise precursor injection, allowing tunable shell thickness and interfacial strain to regulate carrier dynamics. Beyond zero-dimensional systems, seeded epitaxy also guided the formation of metal-semiconductor interfaces, in which preformed metal seeds induced localized semiconductor overgrowth, generating intimate Schottky or Ohmic contacts that facilitated hot-electron injection or interfacial charge extraction. More recently, analogous concepts were extended to construct S-scheme and Z-scheme heterojunctions [2]. One semiconductor acted as a crystalline template that promoted oriented growth of a second phase, thus maximizing interfacial contact area and internal electric field formation. Compared with random or post-synthetic assembly, seeded strategies provided precise spatial control, stronger electronic coupling, and reduced defect density at the junction. Furthermore, the rational modulation of interface geometry tailored band alignment, internal electric fields, and carrier transport pathways. As a result, seed-mediated growth was not merely a morphological control technique but an effective interfacial engineering strategy for designing high-performance heterostructures in photocatalysis and beyond.

3.2 Epitaxial growth

Seed-mediated growth and epitaxial growth are closely related yet conceptually distinct processes in interface construction. In seed-mediated growth, preformed nanocrystals serve as nucleation centers that lower the energy barrier and direct subsequent deposition, primarily governing kinetics and morphology. Epitaxial growth requires several essential thermodynamic and kinetic conditions [56–58]. First, the interfacial energy between the substrate and the overlayer must be sufficiently low to favor layer continuity rather than island formation. Second, lattice mismatch should be limited, typically below 5%, to minimize strain accumulation and enable coherent interfaces. Third, reaction kinetics must be carefully regulated to ensure controlled nucleation and directional crystal propagation. By introducing preformed crystalline seeds, heterogeneous nucleation was preferentially initiated at specific facets, which reduced interfacial energy barriers and suppressed uncontrolled secondary nucleation in solution. This strategy enabled precise regulation of lattice coherence, strain distribution, and epitaxial orientation at the junction, thereby generating intimate and atomically coupled interfaces.

Compared with randomly assembled catalysts, epitaxial growth offered distinct advantages in constructing high-performance photocatalytic materials because it enabled atomically coherent heterointerfaces with minimal defects and well-defined crystallographic relationships (Fig. 4(a)) [52]. Such ordered interfaces facilitated directional charge transfer, suppressed interfacial recombination, and preserved strong redox potentials, thereby improving overall photocatalytic efficiency (Fig. 4(b)) [15]. In addition, epitaxial architectures allowed precise control over shell thickness, exposed facets, and spatial distribution of active sites, enhancing light utilization and reaction selectivity [56]. However, successful epitaxial growth required several stringent conditions. Besides the lattice match, crystallographic symmetry compatibility and similar surface

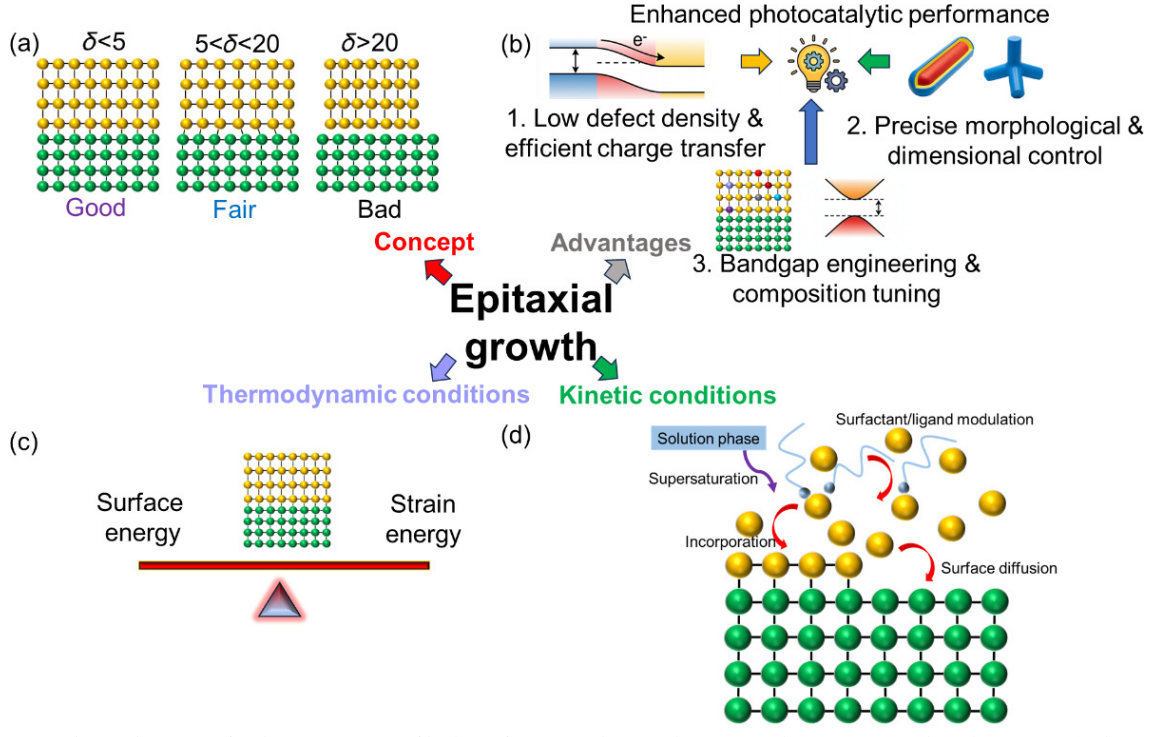

Figure 4 Epitaxial growth strategy for the preparations of high-performance photocatalytic materials. (a) Concept. (b) Advantages. (c) Thermodynamic conditions. (d) Kinetic conditions.

energies were also necessary to guide oriented nucleation (Fig. 4(c)). Moreover, carefully controlled growth kinetics, including precursor concentration, temperature, and solvent coordination, were essential to balance nucleation and lateral growth (Fig. 4(d)). These constraints defined the feasibility and quality of epitaxial photocatalyst synthesis. For example, heteroepitaxial Au@CdS nanoeggs were prepared through selective deposition of hexagonal CdS on Au (111) facets [51]. Similarly, 1D/2D epitaxial CdS/$ZnIn_2S_4$ heterostructures were synthesized via secondary growth of ultrathin $ZnIn_2S_4$ nanosheets on CdS nanowires [46], forming coherent interfaces that facilitated rapid electron delocalization and enhanced photoelectrochemical currents. Epitaxial strategies were also extended to MOF -based systems, where oriented MOF heterostructures were selectively grown on crystalline substrates to establish continuous charge-transport networks [58]. Lattice -matched epitaxial growth of CuS on Bi_2WO_6 nanosheets generated built -in electric fields that promoted electron migration to exposed Cu sites [15]. Overall, epitaxial growth offered decisive advantages by synchronizing structural integrity, optical absorption enhancement, and interfacial charge dynamics.

3.3 Ion-exchange-upgraded nanostructures

Ion-exchange synthesis offered unique advantages for constructing advanced photocatalytic materials because it enabled deep compositional tuning while preserving the parent morphology, crystallinity, and hierarchical architecture (Fig. 5(a)) [59, 60]. Unlike conventional bottom-up routes, ion exchange decoupled structural formation from electronic optimization, allowing well-defined templates to be transformed into new phases without structural collapse [59]. By selectively replacing cations within an intact anionic framework, this strategy provided access to metastable compositions, coherent heterointerfaces, and composition gradients that were difficult to achieve otherwise. Partial ion exchange was particularly powerful for creating core-shell or segmented heterostructures, where internal electric fields enhanced charge separation [61, 62]. The complete ion exchange enabled full phase conversion with inherited porosity and surface area. Taken together, ion exchange is thermodynamically driven by Gibbs free energy (Fig. 5(b)) and solubility differences (Fig. 5(c)). Ionic radii and diffusion rates kinetically dictate reaction speed and morphological preservation. Several representative examples illustrated its versatility. In metal sulfide systems, CdS nanorods were partially converted into CdS@ZnS or $Cu_{2-x}S$/CdS heterostructures via controlled cation exchange [63, 64], which suppressed photocorrosion and improved hydrogen evolution rates by more than one order of magnitude. Similarly, $ZnIn_2S_4$ nanosheets were derived from ZnS templates through sequential In^{3+} exchange, yielding optimized band alignment and abundant sulfur vacancies for enhanced photocatalytic activity [65, 66]. In plasmonic systems, Ag_2S or $Cu_{2-x}S$ nanocrystals were obtained by exchanging Cd^{2+} in CdS, introducing LSPR while retaining nanoscale morphology [67, 68]. A periodic table was constructed with color-coded elements, highlighting those commonly used in the cation-exchange synthesis of photocatalysts (Fig. 5(d)). Ion exchange was also applied to MOF-derived photocatalysts, where metal nodes were selectively replaced to tune redox properties without destroying the porous framework [39, 69]. As for the interface structure and properties, the conventional cases have been elaborately described [59, 61]. Overall, these examples demonstrated that ion-exchange synthesis was a powerful and flexible strategy for producing high-performance photocatalysts by combining structural inheritance with precise electronic and interfacial engineering.

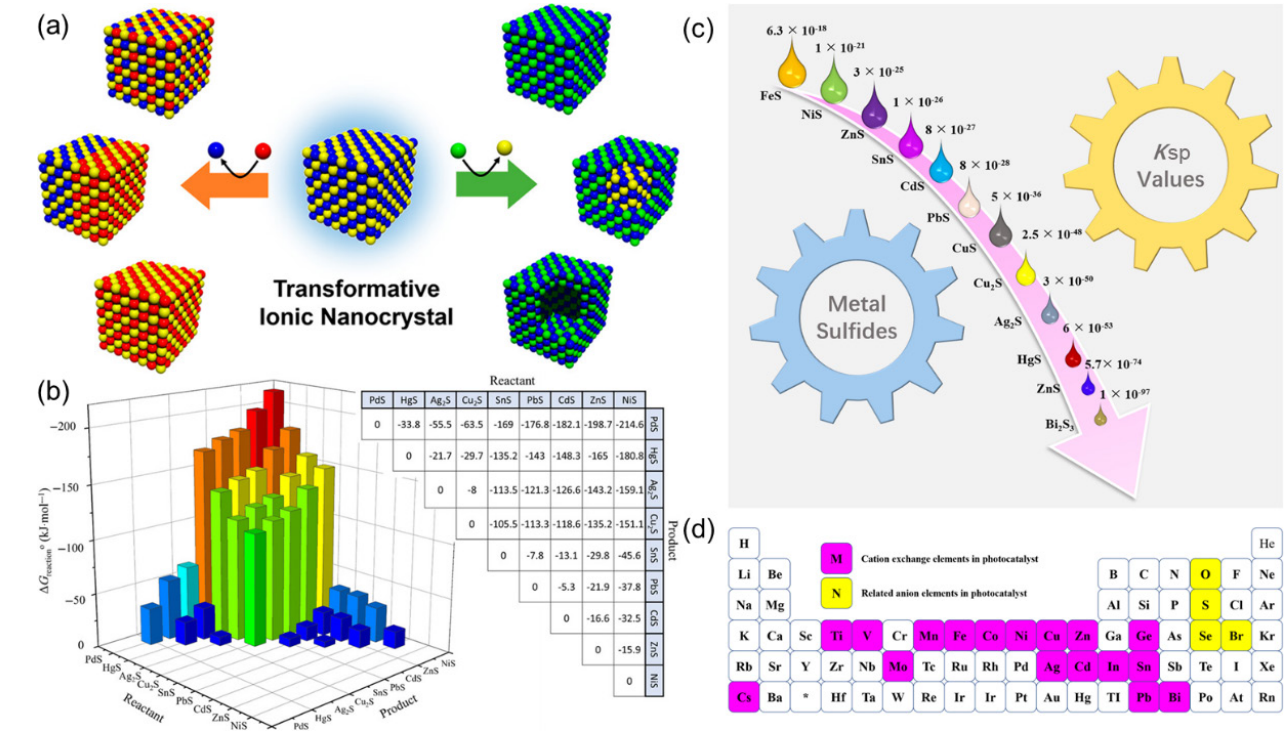

Figure 5 (a) Tuning ionic nanocrystal structures through full and partial ion exchange. Reprinted with permission from Ref. [59], © 2021 American Chemical Society. (b) Thermodynamic comparison of aqueous cation-exchange reactions among metal sulfides. Reprinted with permission from Ref. [60], © 2013 American Chemical Society. (c) Solubility product constants (K_{sp}) of selected metal sulfides. (d) A visual guide to elements for preparing cation-exchange photocatalysts. (c, d) Reprinted with permission from Ref. [61], © 2024 Elsevier Inc.

3.4 Dual-atom catalysts

Atomically dispersed catalysts, i.e., single-atom catalysts (SACs) and dual-atom catalysts (DACs), have been extensively reported owing to their maximized metal utilization efficiency, well-defined coordination environments, and unique electronic structures [37, 70]. DACs can be regarded as a spatially extended evolution of SACs. DACs were generally classified according to the elemental composition and interatomic configuration of the paired sites (Fig. 6(a)) [71]. From the perspective of metal identity, DACs were divided into homonuclear (M-M) and heteronuclear (M-M') types [72]. Homonuclear systems such as Fe-Fe, Cu-Cu, and Ni-Ni emphasized symmetric electronic modulation and metal-metal bond formation, whereas heteronuclear pairs including Fe-Co, Fe-Ni, Cu-In, and Co-Zn introduced asymmetric charge redistribution and orbital coupling effects. According to spatial configuration, dual sites were further categorized into so-called marriage type: metal-metal bonded pairs (2–3 Å), nonmetal-bridged structures (e.g., M-N-M), and adjacent but non-contact sites with medium-range electronic interaction [31]. SACs and DACs generally share analogous synthetic philosophies, as both systems rely on the fundamental principles of atomic dispersion, coordination stabilization, and strong metal-support interaction to prevent aggregation and maintain well-defined active centers. Synthetic strategies primarily involved (Fig. 6(b)) [37, 71]: (i) precursor preorganization in MOFs or COFs followed by pyrolysis to confine paired atoms; (ii) atomic layer deposition or sequential impregnation to construct controllable heteronuclear motifs; (iii) defect engineering or heteroatom anchoring to stabilize dual sites on vacancy-rich supports. In particular, coordination engineering within nitrogen-doped carbon matrices enabled the formation of M_2-N_6 or M-N_4-M' configurations with precise local environments. As for the identification of DACs, characterization techniques precisely identified the geometric and electronic structures of dual-atomic active sites (Fig. 6(c)). Aberration-corrected HAADF-STEM provided high-resolution visual evidence of atomic positions, while X-ray absorption spectroscopy (XAS) revealed average coordination environments and oxidation states. Electron energy loss spectroscopy (EELS) functioned as a powerful complement to distinguish adjacent atoms. Scanning tunneling microscopy (STM) provides high-resolution and visualized surface information at the atomic scale.

Moreover, the choice of support played a decisive role in stabilizing dual sites and regulating photocatalytic pathways. Carbon-based substrates (N-doped graphene, porous carbon, CNTs) provided strong metal-support interactions and flexible coordination environments [13], while two-dimensional semiconductors [73] such as g-C_3N_4, LDHs, MXenes, and transition-metal dichalcogenides facilitated charge separation and interfacial transfer in photo-driven reactions. Representative systems included Fe-Co/N-C for oxygen reduction, Cu-Cu [74], Cu-Ag [75], or Cu-In [76] dual sites for CO_2 reduction with promoted C-C coupling, and Fe-Ni [77] or Ni-Zn [78] motifs for hydrogen or nitrogen conversion reactions. In photocatalytic contexts, dual-atomic-site-integrated g-C_3N_4 [79], CdS [80], and TiO_2 [75, 81] hybrids demonstrated improved H_2 evolution and CO_2 photoreduction due to synergistic adsorption and optimized intermediate stabilization (Fig. 6(d)). Overall, DACs generally outperform SACs by enabling cooperative adsorption and activation at adjacent metal centers. Electronic coupling between paired atoms modulates the d-band structure and intermediate binding strength, potentially overcoming scaling limitations [82]. Moreover, dual sites enhance selectivity, allow higher metal loading, and increase accessible active site density.

3.5 Characterizations of atomic-scale interfaces

The characterization of atomic-scale interfaces in photocatalysis required a combination of structural, electronic, and dynamic probes (Fig. 7) [24], as no single technique was sufficient to resolve both geometric precision and functional behavior. High-resolution imaging techniques were first employed to visualize atomic configurations directly. Aberration-corrected transmission electron microscopy (AC-TEM) and high-angle annular dark-field scanning transmission electron microscopy (HAADF-STEM) enabled identification of lattice registry, atomic continuity, and isolated or paired atomic sites at sub-angstrom resolution (Fig. 7(a)) [13, 82]. For epitaxial interfaces, lattice coherence and interfacial strain were further analyzed through atomic-scale mapping and geometric phase analysis, which clarified whether true atomic continuity rather than simple physical contact had been achieved. However, imaging alone could not fully determine coordination environments or bonding states. Therefore, synchrotron-based spectroscopic techniques played a central role (Fig. 7(b)) [2, 83]. X-ray absorption spectroscopy, including X-ray absorption near-edge structure and extended X-ray absorption

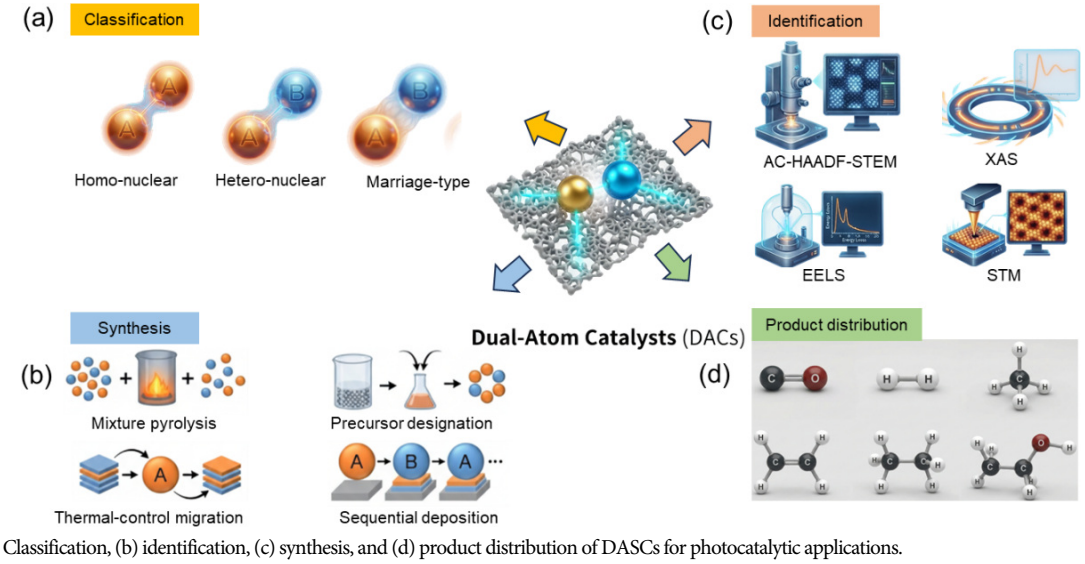

Figure 6 (a) Classification, (b) identification, (c) synthesis, and (d) product distribution of DASCs for photocatalytic applications.

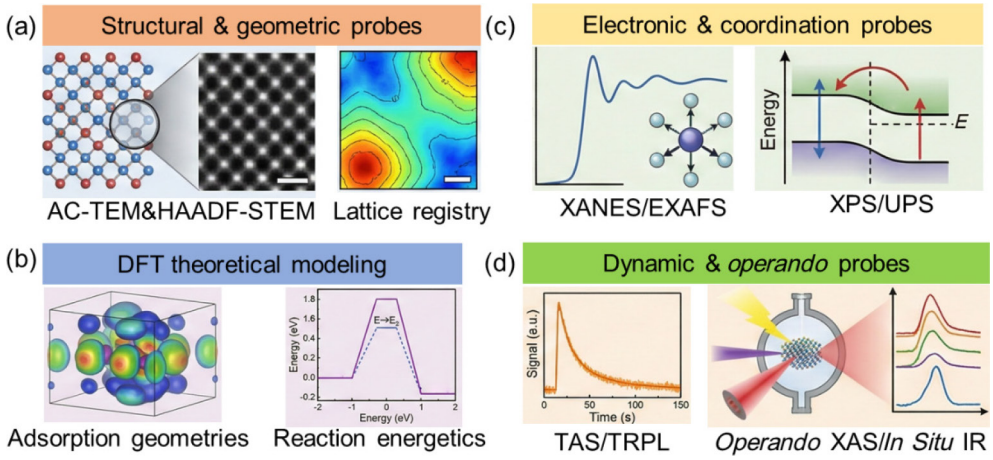

Figure 7 (a) Structural & geometric probes. (b) Electronic & coordination probes. (c) Dynamic & *operando* probes, and (d) DFT theoretical modeling of DASCs for atomic-scale interface analysis.

fine structure analyses, was widely applied to quantify coordination numbers, bond distances, and local symmetry around active atoms. These measurements helped distinguish isolated single atoms from bridged dual-atom ensembles and defect-mediated configurations [12, 84]. X-ray photoelectron spectroscopy and ultraviolet photoelectron spectroscopy were additionally used to evaluate interfacial charge redistribution and shifts in electronic states, revealing evidence of Fermi-level equilibration and built-in electric fields. To probe charge dynamics at atomic-scale interfaces, time-resolved and *operando* techniques were increasingly adopted (Fig. 7(c)). Transient absorption spectroscopy, time-resolved photoluminescence, and surface photovoltage measurements were employed to monitor carrier lifetime, recombination kinetics, and directional charge transfer [38, 85, 86]. *Operando* X-ray absorption and *in situ* infrared spectroscopy provided insights into how interfacial electronic structure evolved under illumination and during catalytic turnover, allowing correlation between atomic arrangement and reaction intermediates [87]. These dynamic measurements were particularly important for identifying reconstruction processes that occurred only under working conditions. Complementing experimental approaches, density functional theory calculations were routinely integrated to model atomic configurations, electronic coupling, and adsorption geometries (Fig. 7(d)) for interpreting spectroscopic observations and rationalize reaction energetics [17, 88]. By combining atomic-resolution imaging, local coordination spectroscopy, time-resolved carrier analysis, and theoretical modeling, researchers gradually established a multidimensional framework to characterize atomic-scale interfaces [89, 90].

4 Engineering atomic-scale interfaces for photocatalytic H_2 evolution and CO_2 reduction

4.1 Epitaxial interfaces

Over the past decade, epitaxial interface engineering has emerged as a decisive strategy to address two central bottlenecks in photocatalytic CO_2 reduction and solar H_2 evolution [51, 52, 91–98]: inefficient charge separation and sluggish interfacial reaction kinetics. The rational lattice matching, coherent bonding bridges, and built-in electric fields could fundamentally reconfigure carrier dynamics at atomic precision. For example, ultrathin $Bi_4O_5Br_2$ nanosheets (BOB) were epitaxially grown on hollow N-doped carbon (NC) spheres (BOB@NC) through an *in situ* oil-bath process, forming robust interfacial Bi-C chemical bonds (Fig. 8(a)) [91]. These covalent bridges acted as atomic-scale electron pumping channels, enabling intimate interfacial contact and a strong built-in electric field. Structurally, the hollow confined architecture enhanced light harvesting via multiple internal reflections and increased CO_2 enrichment. Upon illumination, photogenerated electrons migrated from $Bi_4O_5Br_2$ to the carbon framework through Bi-C bonds and were further trapped at N-induced defect sites, while holes remained in the semiconductor, ensuring directional charge separation (Fig. 8(a)). *In situ* FTIR and DFT analyses revealed that N sites promoted spontaneous CO_2 adsorption and lowered the rate-determining $^*CO_2 \rightarrow ^*COOH$ barrier to 0.41 eV. Under Xe lamp irradiation, the optimized catalyst achieved CO and CH_4 production rates of 28.34 (Fig. 8(b)) and 3.68 $\mu mol \cdot g^{-1} \cdot h^{-1}$ (Fig. 8(c)), corresponding to 3.31- and 11.15-fold enhancements over pristine $Bi_4O_5Br_2$. Similarly, the lattice-match-enabled In_2S_3/CdS Z-scheme heterojunction exhibited an ultralow lattice mismatch of 0.27% and an In-S-Cd covalent bridge, generating a strong built-in electric field that accelerated $2e^-$ oxygen reduction [15]. A 2D/2D p-n heterojunction was fabricated by selectively growing CuS on Bi_2WO_6 nanosheets via a two-step hydrothermal tandem synthesis. This lattice-matched structure created an ultra-fast charge channel [57]. As a result, the formation energy of rate-determining step was reduced from 2.57 to 0.47 eV, yielding CO and CH_4 at rates of 33.9 and 16.4 $\mu mol \cdot g^{-1} \cdot h^{-1}$. Similarly, an S-scheme $(CoCuMgNiZn)O_x@Co_3O_4$ high-entropy oxide (HEO) heterojunction was designed with a minimal lattice mismatch (only 0.90%) [99], facilitating a coherent interface that extended carrier lifetimes by over 100-fold compared to pristine HEO. This architectural precision achieved a CH_4 production rate of 72.38 $\mu mol \cdot g^{-1} \cdot h^{-1}$ with ~90% selectivity under visible light. Beyond C_1 products, the construction of intralattice-bonded asymmetric Bi_1-O-Bi_2 sites at the Bi_3NbO_7(BNO)/Bi_3O_4Br(BOB) interface successfully addressed the C-C coupling bottleneck (Figs. 8(d) and 8(e)) . By inducing interfacial charge redistribution and d-electron feedback, this epitaxial active interface lowered the $2CO^* \rightarrow OCCO^*$ coupling barrier to –0.36 eV (Fig. 8(f)). Consequently, the catalyst exhibited a robust acetic acid production rate of 192.3 $\mu mol \cdot g^{-1} \cdot h^{-1}$ with ~90% selectivity. Collectively, these works demonstrate that engineering epitaxially bonded interfaces not only broadens light-harvesting capabilities but also provides the necessary built-in electric fields to drive complex multi-electron transfers for solar fuel production.

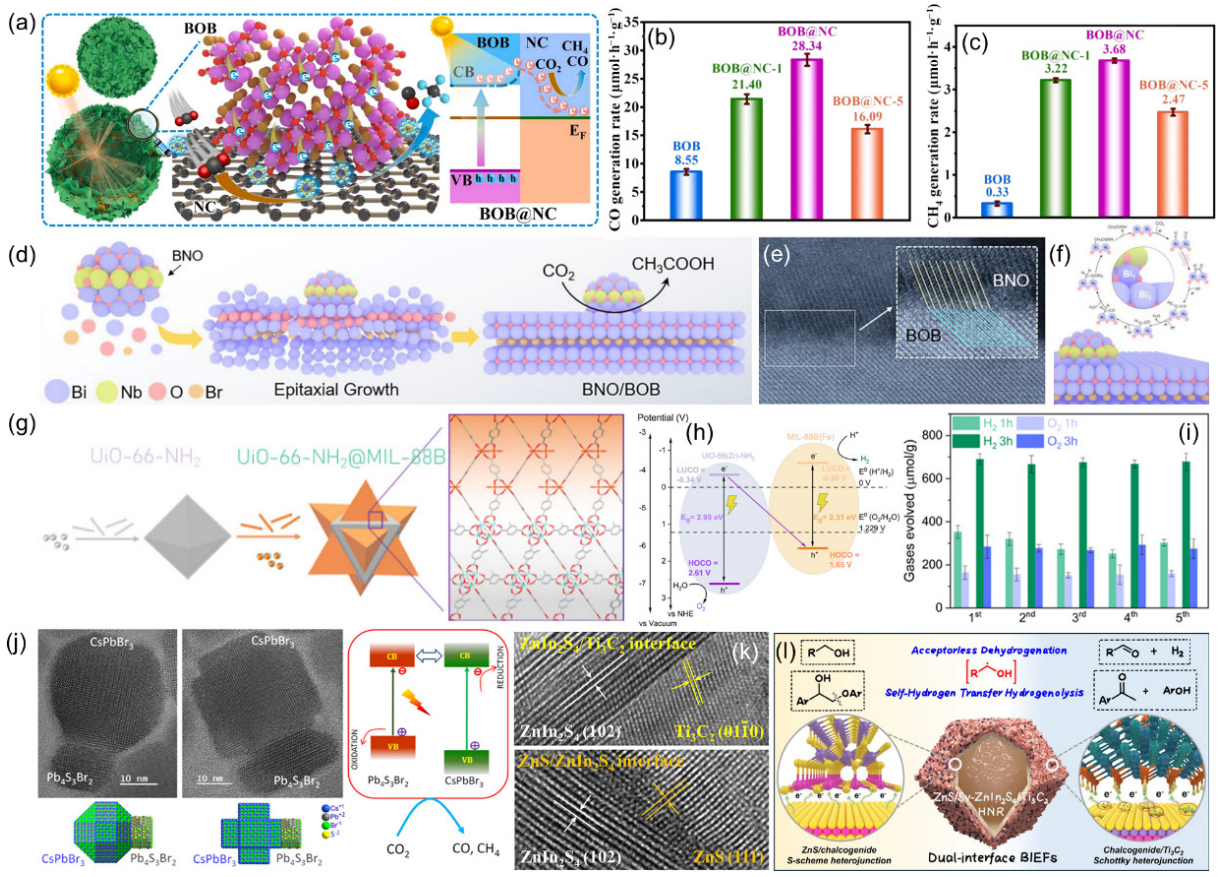

Figure 8 (a) Schematic illustration of CO_2 conversion pathway over $Bi_4O_5Br_2$ (BOB)@ N-doped carbon (NC) hollow confined electron pump photocatalyst. Comparison of average (b) CO and (c) CH_4 evolution rates for NC, BOB, and BOB@NC. (a–c) Reprinted with permission from Ref. [91], © 2025 Elsevier B.V. (d) Schematic formation process of Bi_3NbO_7(BNO)/Bi_3O_4Br(BOB) with lattice-bonded asymmetric Bi_1-O-Bi_2 active sites. (e) HAADF-STEM image of BNO/BOB interface. (f) Schematic illustration of CO_2-to-acetic acid conversion on BNO/BOB photocatalyst. (d–f) Reprinted with permission from Ref. , © 2026 Wiley-VCH GmbH. (g) Two-step synthesis of UiO-66(Zr)-NH_2@MIL-88B(Fe) nanoparticles and interfacial crystal matching between (111) and (001) planes. (h) Proposed Z-scheme photocatalytic mechanism. (i) The performance for five consecutive cycles over UiO-66(Zr)-NH_2@MIL-88B(Fe). (g–i) Reprinted with permission from Ref. [92], © 2024 Huec, T. L. et al. Published by American Chemical Society. (j) Facet-directed epitaxial construction of lead halide perovskite-sulfobromide heterostructures toward improved photocatalytic activity. Reprinted with permission from Ref. [93], © 2022 American Chemical Society. (k) Lattice spacings of 0.31, 0.32, and 0.26 nm corresponding to ZnS(111), $ZnIn_2S_4$(102), and Ti_3C_2(0110) revealed by HRTEM. (l) Dual-interface built-in electric fields within Janus heterostructures for enhanced cooperative photoredox catalysis. (k, l) Reprinted with permission from Ref. [94], © 2025 American Chemical Society.

Facet engineering can also refine carrier pathways. In MOF-on-MOF systems, epitaxial growth of MIL-88B(Fe) on UiO-66(Zr)-NH_2 constructed a face-selective heterointerface with matched (111)/(001) planes through a controlled solvothermal route (Fig. 8(g)) [92, 100]. This precise lattice matching ensured intimate interfacial contact and minimized charge-transfer resistance. The hybrid architecture combined complementary light absorption of both MOFs and introduced a new visible-light absorption tail up to ~650 nm. Upon irradiation, photogenerated electrons in UiO-66(Zr)-NH_2 recombined with holes in MIL-88B(Fe), while high-energy electrons and holes were spatially separated on MIL-88B(Fe) and UiO-66(Zr)-NH_2, respectively, following a Z-scheme pathway (Fig. 8(h)). Under simulated sunlight (AM 1.5G), the heterostructure achieved overall water splitting rates of 690 μmol·g^{-1} H_2 and 279 μmol·g^{-1} O_2 within 3 h (Fig. 8(i)), with apparent quantum yields of ~0.9% at 400–450 nm, markedly outperforming the individual MOFs. Moreover, a secondary building unit (SBU) regulation strategy was employed to synthesize two Ti-MOF phases. The hetero-phase composite of COK and MIL-125 was subsequently assembled [101]. The resulting COK/MIL-125 exhibited superior photocatalytic H_2 evolution compared with the individual phases, which was attributed to the formation of a Z-scheme homojunction at the hetero-phase interface. Further amino functionalization broadened visible-light absorption and markedly enhanced H_2 production. MOF-based hetero-phases enabled periodic porosity and molecular-level band modulation for efficient solar-driven catalysis. As for perovskite nanocrystal heterostructures, facets-directed epitaxial growth was employed to construct lead halide perovskite sulfobromide heterostructures, where lattice-matched domains were selectively grown on specific crystal facets to form strong interfacial chemical bonds (Fig. 8(j)) [93]. This heteroepitaxial strategy minimized interfacial defects and ensured atomic-level continuity through interfacial orbital coupling. The migration and separation of photogenerated electrons were enhanced. The optimized heterostructure exhibited a H_2 evolution rate of 356 μmol·g^{-1}·h^{-1} under visible-light irradiation, demonstrating that facet-controlled epitaxial bonding effectively boosted interfacial charge transport and catalytic efficiency.

Defect-induced epitaxial growth strategies introduced interfacial vacancies or substitutional dopants that tuned band alignment and local charge density, enabling rapid spatial separation of electrons and holes [102]. Multicomponent photocatalysts faced insufficient charge migration driving forces and weak interfacial interactions. A Janus ZnS/Sv-$ZnIn_2S_4$/Ti_3C_2 hollow nanoreactor heterostructure featuring dual-interface built-in electric fields was developed [94].

The strategic design highlight involved establishing a hollow core-shell $ZnS/ZnIn_2S_4$ S-scheme heterojunction through lateral epitaxy, followed by anchoring Ti_3C_2 nanoparticles onto the chalcogenide surface via defect-mediated chemical bonding (Fig. 8(k)). Mechanistically, photogenerated electrons followed an S-scheme pathway across the $ZnS/ZnIn_2S_4$ interface and were subsequently extracted to Ti_3C_2 through a Schottky junction (Fig. 8(l)). The holes accumulated on ZnS, enabling spatially separated redox sites under illumination. As a result, the optimized catalyst delivered hydrogen evolution rate of 751 $\mu mol \cdot g^{-1} \cdot h^{-1}$ and maintained stable activity over multiple cycle. Developing efficient metal-free photocatalysts remained challenging due to the significant energy loss within the interlaminar spaces of conventional van der Waals heterojunctions. A hydrogen-initiated chemical epitaxial growth strategy was proposed to fabricate in-plane graphene/carbon nitride heterostructures [103]. The design highlight involved the *in situ* generation of methane from the hydrogenated decomposition of carbon nitride fragments, which triggered graphene growth specifically along active cyano sites at the edges of confined nanopores. This integration utilized the high lattice symmetry compatibility-with only a 1.4% difference in lattice parameters-to minimize interface resistance. The incorporated nanographene (0.5%) induced a plasmonic effect that extended light harvesting into the full visible and even NIR regions, while simultaneously concentrating the local electrical field at the interface. These in-plane channels facilitated rapid charge carrier migration and suppressed recombination. Consequently, the catalyst achieved a H_2 evolution rate of 7720 $\mu mol \cdot g_{(graphene)}^{-1} \cdot h^{-1}$ without noble metal cocatalysts, representing a 3.7-fold increase in water splitting performance compared to pristine carbon nitride.

Epitaxial interfaces offer strong electronic coupling, efficient charge separation, and fast carrier transport because of their coherent atomic contact and ordered crystallographic alignment. They are especially effective in photocatalytic systems that require directional charge migration and stable interfacial structures. However, their construction often depends on strict lattice matching, compatible crystal symmetry, and precise growth control, which limits material selection and large-scale synthesis. Lattice mismatch may also induce strain, dislocations, or defects that reduce catalytic efficiency. Key unresolved challenges include expanding material universality, controlling strain at the atomic level, understanding dynamic interfacial evolution under reaction conditions, and developing scalable synthetic routes.

4.2 Interfacial chemical bridge interfaces

Interfacial bonding was characterized by the formation of directional chemical bridges (e.g., M-O-M', M-S, or M-P-N) that coupled two components at the atomic scale and reconstructed local electronic structures [104]. Such bonds effectively passivated interfacial defects [105, 106], suppressed carrier recombination [107], and established built-in electric fields [108] through charge redistribution. More importantly, orbital hybridization across the interface created fast electron transport channels and modulated adsorption energetics of key intermediates [109]. In photocatalytic systems, these structurally defined interfaces can synergistically improve activity, selectivity, and long-term stability under illumination [110, 111]].

The simultaneous activation of chemically inert CO_2 and N_2 while suppressing competitive H_2 evolution is intrinsically challenging (Fig. 9(a)). The asymmetric Zn-O-Ti interfacial configuration in MIL-125@ZIF-8 was established to chemically connect ZIF-8 with MIL-125 via a controlled deposition-calcination strategy (Figs. 9(b) and 9(c)), thereby creating atomically coupled heterointerfaces between the two frameworks [108]. Interfacial Zn-O-Ti bridges promoted charge redistribution and generated an internal electric field, accelerating electron transfer from TiO_2 to Zn-coordinated sites (Fig. 9(d)). These sites facilitated CO_2 adsorption and N_2 polarization, enabling C-N coupling at adjacent active centers. As a result, the catalyst achieved a urea formation rate of ~130 $\mu mol \cdot g^{-1} \cdot h^{-1}$ (Fig. 9(e)) with AQY of 5.52% at 350 nm, representing a several-fold improvement over single-component references and demonstrating superior stability over 30 h of continuous illumination. The theoretical calculations suggested that the dominant pathway involved the coupling between *CO and $*NH_2$ intermediates, rather than the alternative $*CHO\text{-}NH_2$ route (Fig. 9(f)). The resulting $*CO\text{-}NH_2$ intermediate then interacted with an additional *NH species, followed by successive proton-electron transfer steps towards the final urea product. A strain-induced strategy was developed to construct a strong Bi-O bonding interface between $Bi_{12}O_{17}Br_2$ (BOB) nanotubes and a Cu porphyrin-based monoatomic layer (PML-Cu) [112]. The design utilized tensile strain to generate abundant surface oxygen vacancies, which acted as anchoring sites for the atomic-scale encapsulation of PML-Cu. This structural engineering enabled broad light absorption and triggered multi-step surface-interface dual polarization, effectively driving electrons from the BOB conduction band to the PML-Cu surface. Consequently, photogenerated electrons enriched at high-density, uniform Cu active sites, facilitating CO_2 activation and CO desorption. The resulting PBOB catalyst achieved a superior CO production rate of 584.3 $\mu mol \cdot g^{-1}$, outperforming pristine BOB by 7.83 times. A hierarchical $In_{4/3}P_2S_6/TiO_2$ S-scheme junction featuring robust P-O interfacial bonding was delicately constructed. Utilizing a two-step hydrothermal-etching process followed by chemical vapor conversion, ultrathin $In_{4/3}P_2S_6$ nanosheets were grown *in situ* onto hollow TiO_2 nanospheres [113]. The unique hollow architecture and strong P-O linkages significantly enhanced light-harvesting capability while providing direct electron-transfer bridges. Driven by a built-in electric field, photogenerated electrons migrated from the TiO_2 conduction band to the $In_{4/3}P_2S_6$ nanosheets, effectively suppressing charge recombination. Spatially separated active sites preserved strong redox potential, enabling the optimized IPST-10 catalyst to achieve a remarkable H_2 evolution rate of 962.9 $\mu mol \cdot g^{-1} \cdot h^{-1}$, approximately 5.7 times that of pristine TiO_2. Similarly, a hierarchical heterostructure featuring coordinated In-N-In interfacial sites was constructed to bridge $ZnIn_2S_4$ and In_2O_3. The synthesis involved the thermal calcination of an In-MOF precursor under nitrogen to produce carbon-coated hollow tubular In_2O_3 (C/HT-In_2O_3), followed by the *in situ* growth of thin-layered $ZnIn_2S_4$ nanosheets [114]. This unique design utilized the In-N-In sites to narrow the C/HT-In_2O_3 band gap to 1.8 eV, effectively transforming a Type-I straddling alignment into a Type-II staggered heterojunction. Consequently, photogenerated electrons migrated across the carbon-bridged interface from C/HT-In_2O_3 to $ZnIn_2S_4$, where high electronic conduction further accelerated the protonation process. The resulting catalyst achieved an optimal hydrogen evolution rate of 920.5 $\mu mol \cdot m^{-2}$ at a 1:2 mass ratio, which was approximately 13.2 times and 6.6 times higher than that of pristine C/HT-In_2O_3 and $ZnIn_2S_4$, respectively.

In order to develop bifunctional photocatalysis with rapid carrier kinetics and promoted redox potentials, an S-scheme

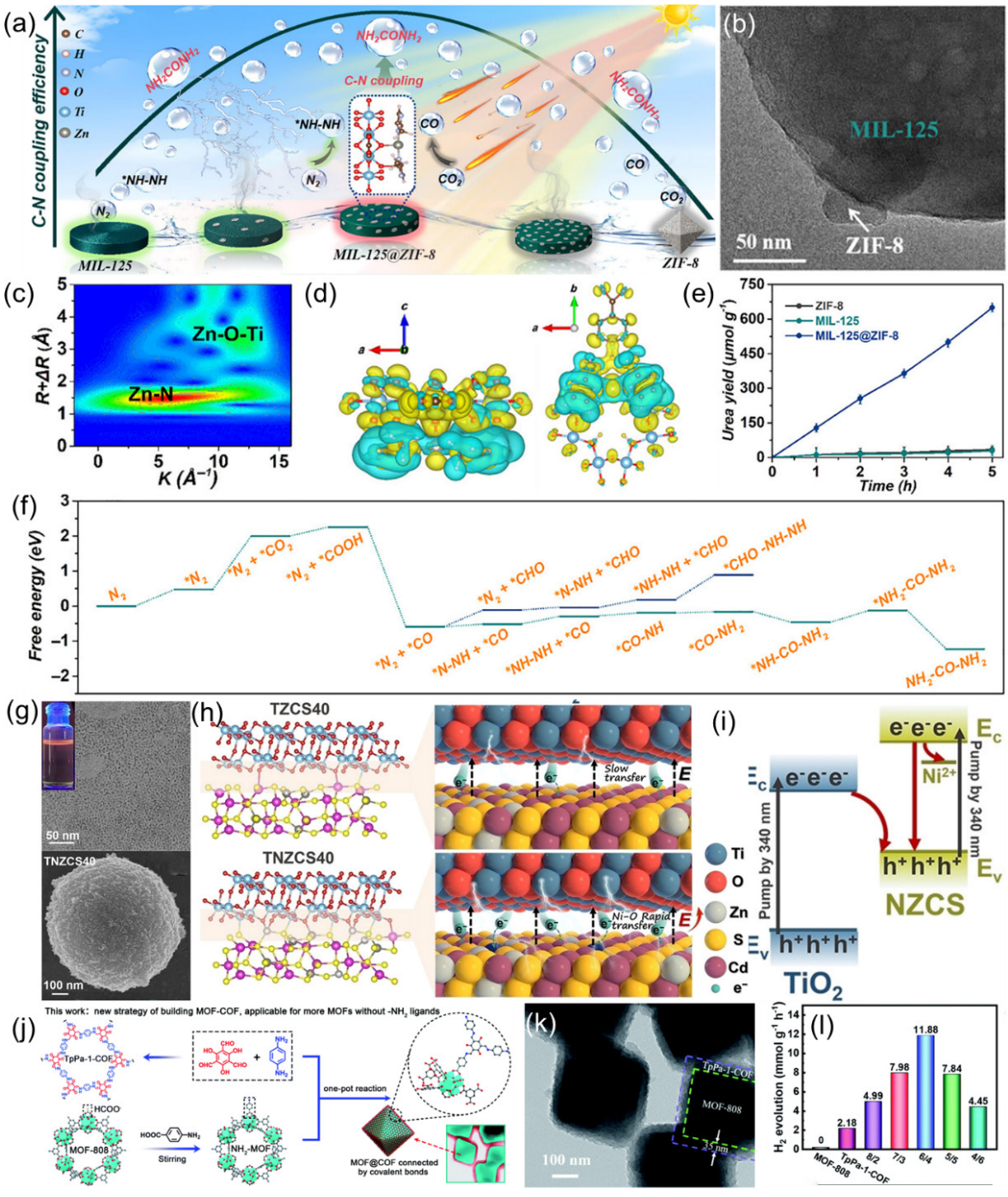

Figure 9 (a) Optimizing ZIF-8 content in MIL-125@ZIF-8 for enhanced C-N coupling activity. (b) TEM image of MIL-125@ZIF-8. (c) K-edge EXAFS. (d) Charge accumulation and depletion at the MIL-125@ZIF-8 interface. (e) Time-dependent yield of urea. (f) Reaction free energy pathways for urea formation over MIL-125@ZIF-8. (a–f) Reprinted with permission from Ref. [108], © 2025 Wiley-VCH GmbH. (g) TEM image of Ni-doped $Zn_{0.2}Cd_{0.8}S$ quantum dots (top) and SEM image of Ni-doped $Zn_{0.2}Cd_{0.8}S$ decorated TiO_2 (TNZCS40, bottom). (h) Schematic illustration of electron migration in TZCS40 and TNZCS40 driven by internal electric fields. (i) Schematic diagram depicting S-scheme charge migration pathway within TNZCS40. (g–i) Reprinted with permission from Ref. [110], © 2023 Wiley-VCH GmbH. (j) A covalent linkage strategy for MOF-808@COF core-shell materials toward improved photocatalytic H_2 evolution. (k) TEM image of MOF-808@TpPa-1-COF. (l) Photocatalytic H_2 evolution activities of MOF-808@TpPa-1-COF-related samples. (j–l) Reprinted with permission from Ref. [111], © 2021 The Royal Society of Chemistry.

heterojunction (TNZCS40) composed of Ni-doped $Zn_{0.2}Cd_{0.8}S$ quantum dots (NZCS QDs) and TiO_2 (T) microspheres was meticulously designed (Fig. 9(g)) [110]. The integration was achieved via a strategic electrostatic self-assembly method, facilitating the formation of robust interfacial Ni-O chemical bonds that acted as atomic-scale highways for rapid charge transfer. This structural configuration significantly extended light harvesting into the visible region and established a strong built-in electric field (Fig. 9(h)), which lowered the interfacial energy barrier from 7.89 to 6.25 eV. Structurally, Ni doping regulated the electronic configuration of surface S sites and weakened H-S bonding. Photogenerated electrons migrated along an S-scheme pathway from TiO_2 to Ni^{2+} states and then to active S sites (Fig. 9(i)). As a result, H_2 evolved on S centers and benzylamine

oxidation proceeded on TiO_2 Lewis acid sites, delivering an H_2 rate of 4.55 mmol·g^{-1}·h^{-1}. Beyond S-scheme charge regulation, atomic-level interfacial reconstruction further enabled overall water splitting by establishing direct metal-chalcogen-metal charge pathways. In MOF and C_3N_4 hybrid system, an NH_x-Zr-O chemically bonded interface was constructed by *in situ* solvothermal growth of NH_2-UiO-66 (NUZ) nanocrystals on NH_x-rich holey g-C_3N_4 (HGN) [115]. The exposed -NH_x groups acted as anchoring "hot spots," enabling uniform dispersion of 30–80 nm MOF particles. This structural integration suppressed the leaching of NUZ and thus promoted the structural stability. The interfacial bonding redistributed π-electrons and slightly red-shifted the absorption edge. Photogenerated electrons migrated from the CB of HGN to NUZ, facilitating CO_2-to-CO conversion. The optimized composite delivered 31.7 μmol·g^{-1}·h^{-1} CO production rate, nearly 2–3 times higher than the single components. In MOF@COF hybrid, a post-synthetic modification strategy was developed. Typically, the acetate ligands on the Zr_6 clusters of MOF-808 were replaced with p-aminobenzoic acid, thereby grafting the surface with reactive -NH_2 groups (Fig. 9(j)) [111]. This enabled the subsequent *in situ* growth of a TpPa-1-COF shell via a Schiff base reaction, forming a robust MOF 808@TpPa-1-COF core-shell heterostructure linked by C-N covalent bridges (Fig. 9(k)). This design preserved high crystallinity and porosity while creating a continuous electronic pathway across the interface. Upon irradiation, photogenerated electrons migrated directionally from the COF to the MOF through the covalent linkage, while holes were efficiently scavenged by sacrificial agents, forming a type-II charge-transfer pathway. Hydrogen evolution proceeded on Pt-decorated MOF sites under $\lambda > 420$ nm illumination. Consequently, the optimized catalyst achieved a hydrogen evolution rate of 11.88 mmol·g^{-1}·h^{-1} (Fig. 9(l)) and an apparent quantum efficiency of 10.2% at 450 nm, far outperforming non-covalent counterparts. Constructing interfacial N-Bi-N chemical bonds through dinitrogen-chelating ligands in the interface of ultrathin MOF and single-rod $Cs_3Bi_2Br_9$ nanocrystals served as a high-speed electron bridge [116]. Photogenerated electrons migrated from Bi-centered units to the surrounding framework through N-Bi-N bridges, markedly lowering interfacial charge-transfer resistance and suppressing recombination. The polarized N-Bi-N sites also optimized *CO_2 activation and *CO intermediate stabilization, demonstrating a decisive motif for high-efficiency photocatalysis.

To address the challenge of constructing efficient charge-transport channels in multi-component photosystems, an organic-inorganic hybrid cocatalyst system with tunable interfacial structures was developed [117–119]. The design utilized a two-step photochemical deposition and *in situ* polymerization to grow polyaniline (PANI) monolayers and Pt nanoparticles on CdS, strategically engineering S-C, S-Pt, and Pt-N chemical bonds [119]. The formation of these adequate interfacial linkages established direct pathways for photogenerated electrons to migrate from the CdS semiconductor to the synergistic cocatalysts. This structural orchestration effectively suppressed carrier recombination, as evidenced by a doubled charge lifetime (0.24 ns) in the optimized configuration. The reaction followed a typical water-reduction pathway, where Pt served as the proton reduction site while PANI promoted interfacial electron injection. As a result, an apparent quantum efficiency of 92.1% at 440 nm was achieved, 84 times higher than pristine CdS, confirming that tailored interfacial bonding governed carrier dynamics and catalytic efficiency. A TiO_2/CdS/Ni (CSTNi) core-shell S-scheme photocatalyst was designed, by utilizing a sequential hard-template method (Fig. 10(a)). The orchestrated precise interfacial Ti-S and Ni-S chemical bonds served as high-speed electron transport channels [117]. The design highlight resided in the d-p orbital hybridization between transition metals (Ti and Ni) and sulfur (Fig. 10(b)), which modulated the local electronic structure and lowered interfacial energy barriers. While the hollow nanosphere structure enhanced light utilization through internal cavities, the staggered band alignment drove photogenerated electrons from the TiO_2 conduction band to recombine with CdS holes, effectively preserving the strong oxidative power of TiO_2 and the reductive potential of CdS (Fig. 10(c)). Ni nanoparticles acted as specific active sites, enriching electron density through a Ni-S bonded Schottky barrier to facilitate H_2 evolution. Consequently, CSTNi delivered a remarkable hydrogen evolution rate of 1126.9 μmol·g^{-1}·h^{-1} in a microplastic-containing alkaline solution (Fig. 10(d)), demonstrating its superior capability for coupled clean energy conversion and environmental remediation. The MoS_2 cocatalysts suffered from the intrinsic limitation of overly strong S-H* adsorption that hindered hydrogen desorption and slowed H_2 evolution kinetics (Fig. 10(e)). To overcome this challenge, a core-shell Ag@MoS_2 cocatalyst featuring Ag-S bonding interfaces was constructed on TiO_2 via a two-step photodeposition route, in which metallic Ag nanoparticles were first deposited and subsequently coated with an amorphous MoS_2 shell (Fig. 10(f)) [109]. The key design lay in Ag-induced p-orbital electron modulation of S atoms. Free electrons directionally transferred from the Ag core to the MoS_2 shell, generating electron-rich $S^{(2+\delta)-}$ sites (Fig. 10(g)). Structurally, the core-shell configuration preserved TiO_2 light absorption while introducing Ag plasmonic response around 540 nm and efficient interfacial electron sinks. Under irradiation, photogenerated electrons migrated from TiO_2 to Ag and then to MoS_2, where optimized S sites facilitated H* adsorption-desorption with a reduced ΔG_{H^*} from –0.73 to –0.24 eV. As a result, the optimized photocatalyst achieved a high H_2 evolution rate of 1035.3 μmol·g^{-1}·h^{-1} with an apparent quantum efficiency of 3.06%, outperforming TiO_2/Ag and TiO_2/MoS_2 counterparts and demonstrating efficient and stable photocatalytic hydrogen production.

Vacancy engineering enabled the creation of coordinatively unsaturated sites that acted as atomic anchors for forming strong interfacial chemical bonds, thereby promoting intimate interface contact and accelerating directional charge transfer [17]. A sulfur-vacancy-rich $ZnIn_2S_4$/$MoSe_2$ heterostructure was fabricated via a defect-induced *in situ* growth strategy (Fig. 10(h)), in which unsaturated S sites anchored Mo species to form robust interfacial Mo-S chemical bonds (Figs. 10(i) and 10(j)) [118]. This atomic-level bonding, together with the work-function mismatch, established an internal electric field that directed photogenerated electrons to follow a direct Z-scheme pathway (Fig. 10(k)). The hierarchical 2D/2D architecture enhanced visible-light absorption (bandgap narrowed from 2.35 to 2.19 eV). Under illumination, electrons in $MoSe_2$ recombined with holes in $ZnIn_2S_4$, while high-energy electrons accumulated on $ZnIn_2S_4$ to drive H_2 evolution. Using ascorbic acid as a sacrificial agent under $\lambda > 420$ nm irradiation, the optimized photocatalyst achieved a hydrogen evolution rate of 63.21 mmol·g^{-1}·h^{-1}, nearly 18.8 times that of pristine $ZnIn_2S_4$, and delivered an apparent quantum yield of 76.48% at 420 nm. Interfacial Mo-S chemical bonds also created a robust S-scheme heterojunction via vacancy-assisted growth of 2H-$MoTe_2$ on sulfur-vacancy-rich Sv-In_2S_3 substrates [120]. This unique structure enhanced light harvesting through multiple

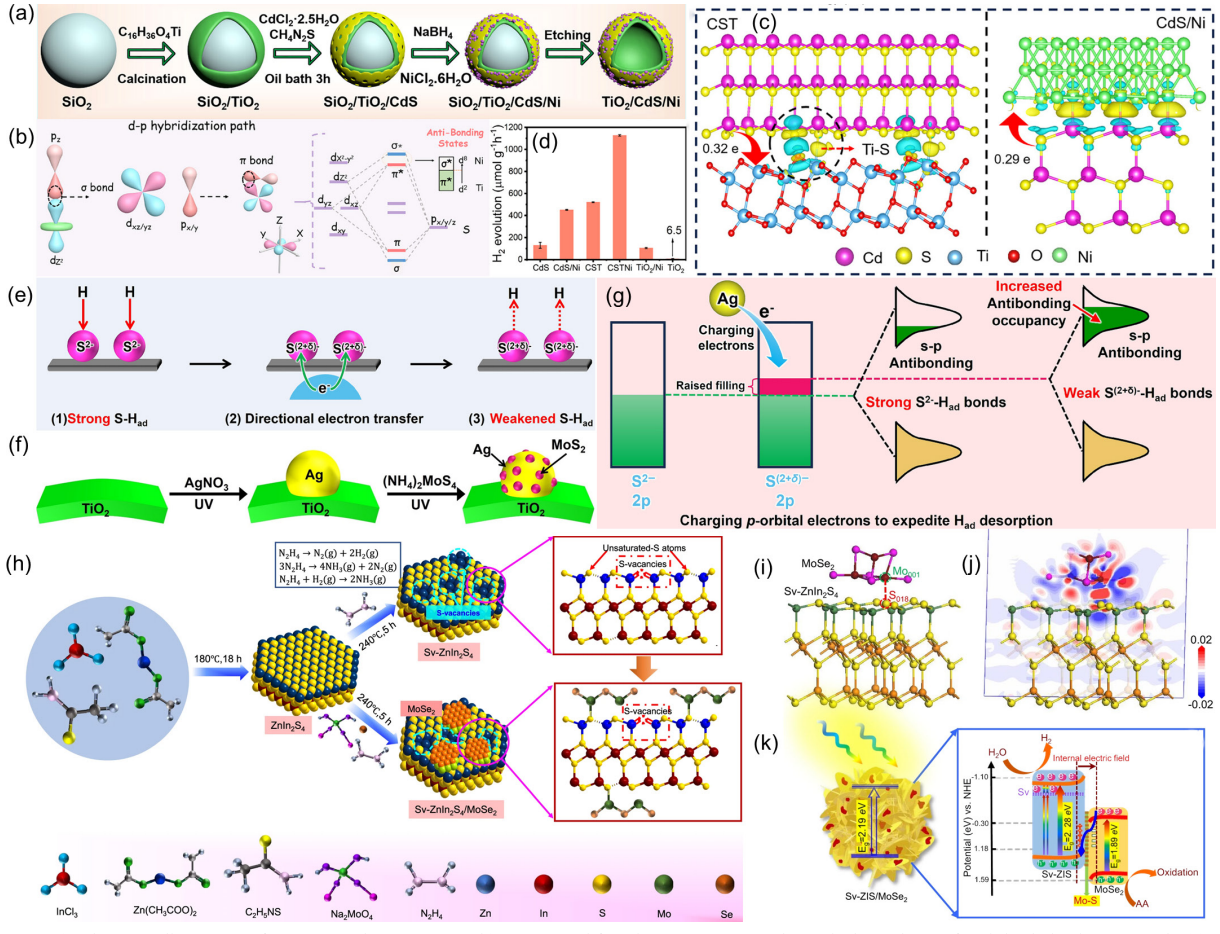

Figure 10 (a) Schematic illustration of CSTNi synthesis process. (b) Engineered fast electron transport channels through interfacial d-p hybridization path. (c) Charge carrier transfer mechanism mediated by Ti-S and Ni-S bonds. (d) Photocatalytic hydrogen evolution activity of CSTNi-related samples. (a–d) Reprinted with permission from Ref. [117], © 2026 Wiley-VCH GmbH. (e) Balancing H adsorption on sulfur sites. (f) Schematic representation of core-shell Ag@MoS_2 modification on TiO_2 photocatalysts. (g) Charging p-orbital electrons to weaken S-H_{ad} bonds via antibonding occupancy. (e–g) Reprinted with permission from Ref. [109], © 2025 Elsevier B.V. (h) Schematic illustration of the synthesis pathway for sulfur-vacancy-rich $ZnIn_2S_4/MoSe_2$ heterostructure. (i) Structural optimization, (j) charge density difference, and (k) photocatalytic mechanism of sulfur-vacancy-rich $ZnIn_2S_4/MoSe_2$. (h–k) Reprinted with permission from Ref. [118], © 2021 Wang, X. H. et al.

scattering effects and established a strong built-in electric field. Photoexcited electrons migrated across polarized Mo-S bridge, lowering *OCHO/*CHO energy barriers and accelerating CO_2 reduction reaction. To further highlight the effectiveness of interfacial chemical bond engineering for high-performance photocatalysis, a MoS_2/defect-rich BiOCl heterointerface through an oxygen-vacancy-assisted self-assembly strategy, followed by selective deposition of Pd on the lateral facets. During the interfacial reconstruction process, sulfur atoms from MoS_2 occupied oxygen-vacancy sites on the BiOCl (001) surface, forming a directional Mo-S-Bi atomic bridge that enabled efficient metal-to-metal charge transfer [105]. This well-defined interfacial bonding pathway promoted interfacial electron migration and effectively suppressed charge recombination. As a result, the MoS_2/Pd-bonded defect-rich BiOCl exhibited simultaneous H_2 and O_2 evolution under neutral conditions without sacrificial agents, demonstrating its capability for efficient overall water splitting driven by atomic-level interfacial charge and energy transfer.

Interfacial chemical bridge interfaces offer distinct advantages because direct chemical bonding between two components can strengthen electronic coupling, accelerate directional charge transfer, and improve structural stability. They are particularly effective in heterostructures where conventional physical contact gives weak interaction or severe carrier recombination. However, their intrinsic limitations include difficult control over bond type, bonding density, and interfacial uniformity during synthesis. Excessive or unstable bonds may also distort local structures or create recombination centers. This strategy is most effective when strong interfacial communication and rapid carrier migration are required. The unresolved challenges include precise atomic-level construction, reliable characterization of bridge bonds under working conditions, and understanding how specific bond motifs regulate catalytic activity and selectivity.

4.3 Organic-inorganic bonded interfaces

Organic-inorganic bonded interfaces offered distinct advantages in photocatalysis by integrating the complementary merits of molecular precision and robust semiconductors [121, 122]. The organic component provided tunable frontier orbitals and specific adsorption sites, while the inorganic phase ensured broad light absorption and efficient photocarrier generation. Through covalent [123], coordination [124], or hydrogen-bond [125] interactions, interfacial bonding established accelerated electron transfer channels across nanometer-scale distances [126–128]. As a result, photogenerated electrons preferentially migrated to molecular active centers, steering reaction pathways and suppressing competing side reactions. Such interfaces enabled

strong electronic coupling, which facilitated directional charge separation and reduced interfacial resistance without sacrificing structural stability. These synergistic effects collectively enhanced quantum efficiencies, improved product selectivity, and enabled photocatalytic rates.

The molecular-semiconductor hybrids suffer from inefficient interfacial charge transfer. Covalently grafting cobalt phthalocyanine (CoPc) onto CdSe quantum dots (QDs) was developed in an organic-inorganic system. The molecular heterojunction was constructed by covalently anchoring CoPc-NH_2 onto CdSe QDs through *in situ* formed dithiocarbamate (-$NHCS_2$) linkages (Fig. 11(a)) [124], which was prepared through a condensation reaction between amino-substituted CoPc and CS_2 in an alkaline environment, followed by *in situ* coordination with Cd surface atoms. The -$NHCS_2$ bond strengthened interfacial coupling and created a robust and directional electronic bridge. The induced built-in electric field promoted electron flow from the CB of CdSe to the LUMO of CoPc-NH_2 (Fig. 11(b)). Electrons accumulated at Co-N_4 sites to drive the *COOH-mediated CO_2-to-CO pathway (Fig. 11(c)), while holes were consumed by sacrificial electron donor. Consequently, the optimized system delivered 3,687 μmol·g^{-1}·h^{-1} CO, 31 times higher than pristine CdSe, demonstrating the decisive role of covalent interfacial engineering. A high-throughput electron transfer pathway at an inorganic-organic interface was engineered to alleviate the competing hydrogen evolution in photocatalytic CO_2 reduction. By functionalizing CdS nanorods with carboxyl (-COOH) groups (Fig. 11(d)) [123], a negatively charged surface was established, which created a strong attractive electric field with the Co(II) bipyridine complexes (Co(II)-bpy) catalytic center (Fig. 11(e)). This configuration contrast significantly with -NH_2 functionalization, which generated a repulsive interface that hindered charge migration. Spectroscopic evidence confirmed that the -COOH modification accelerated electron injection kinetics from CdS to Co(II)-bpy and indicated high-throughput electron delivery. These electrons preferentially populated the molecular orbitals of Co centers, steering the reaction toward a *COOH-mediated CO_2 reduction pathway rather than proton reduction (Fig. 11(f)). As a result, the optimized CdS-COOH/Co(II)-bpy system achieved a CO evolution rate of 2.523 mmol·g^{-1}·h^{-1} (Fig. 11(g)) with 96.3% selectivity and an apparent quantum yield of 1.20% at 420 nm under a mixed acetonitrile, water, and TEOA, demonstrating efficient suppression of H_2 evolution and superior catalytic performance. To address the intrinsic limitation of Bi_2WO_6 in

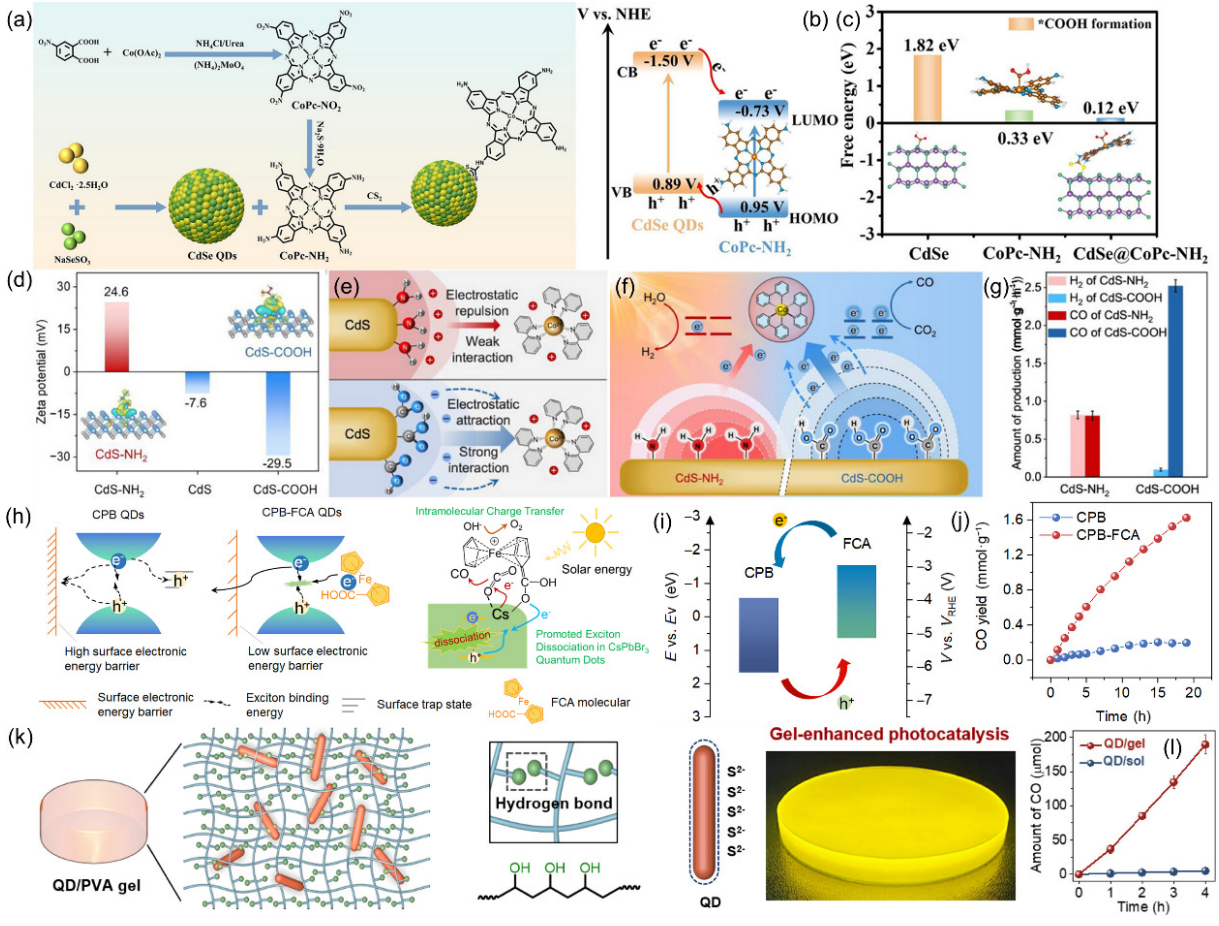

Figure 11 (a) Schematic representation of the synthetic route for CdSe@CoPc-NH_2. (b) Energy band configuration of CdSe@CoPc-NH_2 heterojunction. (c) Calculated *COOH formation energy of CdSe@CoPc-NH_2-related samples. (a-c) Reprinted with permission from Ref. [124], © 2025 Wiley-VCH GmbH. (d) Surface zeta potential measurements for CdS-COOH, CdS-NH_2, and pristine CdS. (e) Interfacial electronic coupling between surface-modified CdS and Co(II)-bpy. (f) Efficient electron transfer mechanism at inorganic-organic interface for selective CO_2 photoreduction. (g) Photocatalytic CO_2 reduction over CdS-COOH/Co(II)-bpy and CdS-NH_2/Co(II)-bpy under visible light. (d-g) Reprinted with permission from Ref. [123], © 2025 Wiley-VCH GmbH. (h) Schematic illustration of exciton dissociation and electron transfer in CPB-FCA upon excitation. (i) Band alignment of CPB and FCA showing electron transfer from FCA to CPB and hole transfer from CPB to FCA. (j) Time-dependent CO production over CPB and CPB-FCA for 18 h. (h-j) Reprinted with permission from Ref. [127], © 2024 Du, C. Y. et al. Published by PNAS. (k) The structure and picture of photocatalyst QD/gel. (l) Time-dependent CO_2-to-CO conversion rate. (k, l) Reprinted with permission from Ref. [125], © 2025 American Chemical Society.

CO_2 photoreduction, an atomic-level W-Cl donor-acceptor structure was constructed by introducing an asymmetric W-Cl anion layer, which induced uneven electron density distribution within the lattice. The W centers acted as electron donors, while adjacent Cl-coordinated sites functioned as acceptors, creating an internal electrostatic potential that promoted directional carrier migration [128]. This built-in polarization accelerated interfacial charge separation and suppressed recombination. Density functional calculations revealed that the energy barrier for *COOH formation was significantly lowered, making the CO pathway thermodynamically preferred. *In situ* FTIR further confirmed stabilized *COOH intermediates. As a result, the modified catalyst achieved a CO yield of 32.11 $\mu mol \cdot g^{-1} \cdot h^{-1}$, nearly four times higher than pristine Bi_2WO_6, demonstrating the decisive role of atomic-level donor-acceptor engineering.

The restricted multiple-exciton dissociation and inefficient charge transfer typically limit the performance of perovskite quantum dots (QDs) in CO_2 reduction. To overcome these barriers, a facile ligand exchange was employed to implement surface engineering by grafting ferrocene carboxylic acid (FCA) ligands onto $CsPbBr_3$ (CPB) QDs, creating a robust intramolecular charge transfer (ICT) bridge (Fig. 11(h)) [127]. Specifically, ferrocene carboxylic acid anchored onto the $CsPbBr_3$ surface via Cs-O coordination between surface Cs^+ sites and the -COOH group of the ferrocene ligand. This interfacial bonding preserved the perovskite lattice while replacing long-chain oleic acid ligands. The FCA was utilized as a dielectric screening agent and microelectric field modulator, which significantly enhanced light harvesting and reduced the exciton binding energy. Under simulated solar illumination, photogenerated electrons spontaneously migrated from the electron-rich FCA ligand to the $CsPbBr_3$ core via Cs anchoring sites (Fig. 11(i)), effectively lowering surface energy barriers. This unique interface facilitated a nine-fold improvement in activity, achieving a record-high CO production rate of 132.8 $\mu mol \cdot g^{-1} \cdot h^{-1}$ (Fig. 11(j)) with 96.5% selectivity in a gas-solid reaction system. As for CdSe/CdS quantum dots, natural photosynthesis in viscous biological environments was referred. A gel-based platform was developed by embedding S^{2-}-capped CdSe/CdS quantum dots into physically cross-linked poly(vinyl alcohol) gels, where abundant hydrogen bonding formed spontaneously between surface S^{2-} ligands and PVA-OH groups (Fig. 11(k)) [125]. This noncovalent interfacial bonding stabilized uniform QD dispersion and constructed a three-dimensional hydrogen-bond network without altering the intrinsic band structure. Femtosecond spectroscopy showed that hydrogen bonding prolonged long-lived charge carriers, thereby promoting efficient electron accumulation at QD surfaces. CO_2 reduction proceeded via *COOH intermediates on QD sites. Consequently, the gel catalyst achieved a CO evolution rate of 94.9 $mmol \cdot g_{QDs}^{-1} \cdot h^{-1}$ under $\lambda \geq 420$ nm irradiation with TEA as a sacrificial agent (Fig. 11(l)), nearly 38 times higher than its solution counterpart, demonstrating the decisive role of hydrogen-bonded interfacial confinement.

Organic-inorganic bonded interfaces combine the robust stability of inorganic semiconductors with the tunable functionality of organic components, enabling improved light harvesting, selective adsorption, and directional charge transfer. They are most effective in systems requiring surface microenvironment regulation or molecular-level reaction control. However, weak interfacial durability, limited long-term stability, and complex charge-transfer pathways remain intrinsic limitations. The persisting challenges include precise bond construction, enhanced resistance to photocorrosion, and deeper understanding of dynamic interfacial interactions under working conditions.

4.4 Dual-atom interfaces

DACs have emerged as an advanced platform in photocatalysis by integrating cooperative adsorption sites with directional charge -transfer channels. Unlike isolated single atoms, paired metal centers enabled synergistic modulation of surface thermodynamics and carrier dynamics. Recent studies demonstrated that rationally engineered dual-atom motifs on carbon nitride, metal oxides, and sulfides significantly enhanced hydrogen evolution and CO_2 reduction. By tailoring coordination environments and electronic coupling, DACs simultaneously optimized light harvesting, intermediate stabilization, and multi-electron reaction pathways.

Photocatalytic H_2 production required efficient light absorption, rapid carrier separation, and minimized proton reduction barriers [129–132]. Dual-atom catalysts addressed these challenges by integrating spatially adjacent redox centers and modulating local electronic density. The Ru-In dual-single atoms on ultrathin TiO_2 nanosheets (Ru-In SA/TiO_2) were prepared for achieving efficient photocatalytic H_2 evolution from pure water without sacrificial agents (Fig. 12(a)) [129]. The catalyst was synthesized via a solvothermal route in which $RuCl_3$ and $InCl_3$ were co-introduced during TiO_2 formation, leading to atomically dispersed Ru-O and In-O coordination. The dual doping significantly enriched Ti^{3+} species and oxygen vacancies. Under 300 W Xe lamp irradiation in pure water, the H_2 evolution rate reached approximately 18,000 $\mu mol \cdot g^{-1} \cdot h^{-1}$ (Fig. 12(b)), which was 53 times higher than pristine TiO_2. Mechanistically, Ru sites catalyzed proton reduction, whereas In sites facilitated hole extraction and water oxidation, enabling efficient redox decoupling and suppressing recombination (Fig. 12(c)). To overcome the intrinsic scaling limitation and insufficient stability of single-atom Pt catalysts in ammonia borane (AB) hydrolysis, Pt-Co dual-single atoms on graphitic carbon nitride were precisely constructed via a stepwise photoinduced anchoring strategy (Fig. 12(d)) [130]. Light irradiation first anchored Co atoms through N lone pairs, and the photoexcited electrons accumulated at Co sites subsequently reduced and immobilized Pt species nearby, forming Pt-Co pairs with an average distance of ≈2.45 Å. The dual sites modulated the band structure, slightly narrowing the bandgap to 2.80 eV and generating a more negative conduction band, thereby enhancing visible-light utilization and electron migration. As a result, the PtCo catalyst achieved a remarkable TOF of 3130 $mol_{H_2} \cdot mol_{Pt}^{-1} \cdot min^{-1}$ (Fig. 12(e)) at 298 K, 3.2 times higher than Pt single atoms, demonstrating superior activity and durability. Charge redistribution from Co to Pt facilitated H_2O activation and optimized AB adsorption (Fig. 12(f)). Conventional Pt cocatalysts suffer from the limited synergy and sluggish interfacial electron transfer, asymmetric B-Pt-O coordination sites were engineered through controlled coordination modulation on a B and Pt co-modified TiO_2 photocatalyst ($Pt_{SA/NP}$-$TiO_{2-x}B_x$) (Fig. 12(g)) [131]. The adjacent $Pt^{\delta+}$-Pt^0 configurations were modulated by sequential photodeposition and coordination regulation. The asymmetric coordination redistributed charge density and created an internal electric field that facilitated directional electron migration from the photoexcited semiconductor to metallic Pt centers. Ultrafast spectroscopy revealed the accelerated carrier separation, prolonged lifetime, and suppressed recombination. Under simulated solar irradiation with sacrificial agents at 40 °C, the optimized catalyst

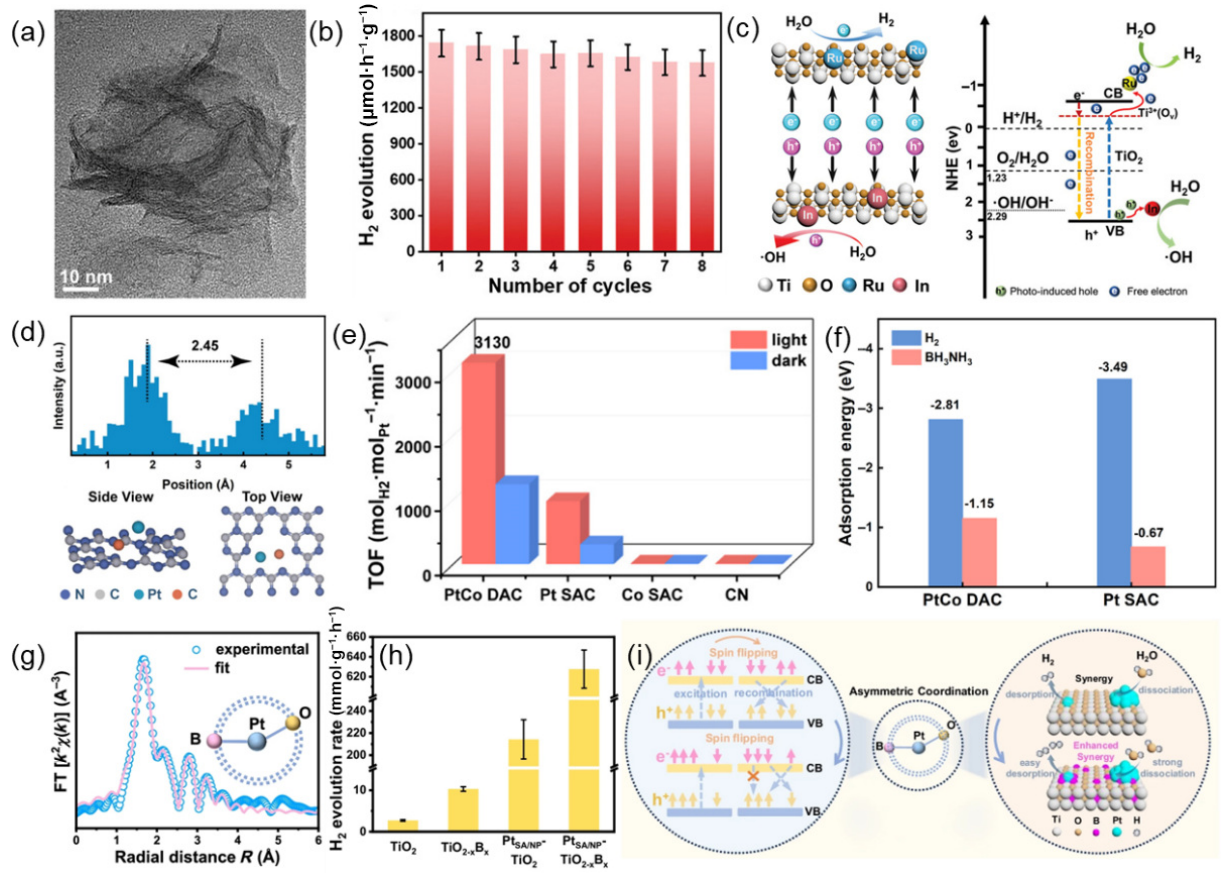

Figure 12 (a) TEM image of Ru-In SA/TiO_2. (b) Recycling tests of photocatalytic H_2 generation over Ru-In SA/TiO_2 (1 h per cycle). (c) Electron-hole dissociation at Ru/In dual-atom decorated TiO_2 surface. (a–c) Reprinted with permission from Ref. [129], © 2022 Wiley-VCH GmbH. (d) Statistical Pt-Co distances and structural models of PtCo dual-atom catalyst (DAC). (e) Light-dependent TOF estimates for all synthesized catalysts under visible illumination. (f) Calculated adsorption energies of H_2 and AB molecules on PtCo DAC and Pt SAC photocatalysts. (d–f) Reprinted with permission from Ref. [130], © 2024 American Chemical Society. (g) Asymmetric coordination of B-Pt-O. (h) Photocatalytic H_2 evolution activity in $Pt_{SA/NP}$-TiO_2 and $Pt_{SA/NP}$-$TiO_{2-x}B_x$. (i) Proposed spin polarization effect boosting charge separation and photocatalytic H_2 evolution activity in $Pt_{SA/NP}$-TiO_2 and $Pt_{SA/NP}$-$TiO_{2-x}B_x$. (g–i) Reprinted with permission from Ref. [131], © 2025 Li, B. et al.

achieved a hydrogen evolution rate exceeding 627.6 mmol·g^{-1}·h^{-1} (Fig. 12(h)), nearly 3 times higher than single-Pt counterparts. Mechanistically, $Pt^{\delta+}$ sites promoted water activation, while Pt^0 centers served as proton reduction sites, enabling cooperative adsorption and efficient H-H coupling with reduced activation barriers (Fig. 12(i)). Noble-metal-free Mn-Co dual atoms were anchored on crystalline carbon nitride [133]. The MnCo sites were generated via co-polymerization and subsequent thermal activation. The heteronuclear configuration facilitated charge delocalization across adjacent metal centers. Hydrogen evolution rates approached 14,092.7 μmol·g^{-1}·h^{-1}, nearly six times that of bulk carbon nitride. The Mn site promoted water dissociation, while Co stabilized hydrogen intermediates. To overcome sluggish interlayer charge transfer in van der Waals heterojunctions, Co dual-atom sites between $ZnIn_2S_4$ and thiol-modified g-C_3N_4 via a thiol-assisted coordination and electrostatic self-assembly strategy. The confined Co dimers formed axial Co-S and in-plane Co-N coordination, preserving the conjugated framework while constructing a sandwich-like dual-Z-scheme. This configuration broadened visible absorption (bandgap reduced to 2.64 eV) and built an internal electric field that drove directional carrier migration. Under 420 nm irradiation with TEOA, the optimized catalyst achieved 15.99 mmol·g^{-1}·h^{-1} H_2 evolution, demonstrating that Co dual-atoms acted as efficient electron bridges to accelerate interlayer delocalization and suppress recombination. A PtAg dual-atom catalyst on CdS nanorods was developed to overcome slow methyl C-H activation and charge recombination. By engineering a PtAg-S bridge unit, an internal electric field was created to direct electrons to Pt for H_2 evolution and holes to Ag for toluene oxidation. This lowered the reaction barrier from 3.02 to 1.31 eV. Consequently, the PtAg DAC achieved 89.8 μmol·g^{-1}·h^{-1} of H_2 and 32.8 μmol·g^{-1}·h^{-1} of 1,2-diphenylethane, significantly outperforming single-atom counterparts. Together, hydrogen evolution systems showed that dual atoms enhanced both thermodynamic adsorption balance and photogenerated electron flux [134]. One atom frequently facilitated H_2O dissociation and the other optimized H* coupling. Dual sites reduced kinetic barriers and stabilized transient intermediates without sacrificing redox potential.

CO_2 photoreduction demanded efficient CO_2 activation, multi-electron transfer, and C-C coupling stabilization [135, 136]. Dual-atom motifs were particularly advantageous in coordinating *COOH, *CO, and multicarbon intermediates [137]. A representative noble-metal-free Ni-W dual-atom catalyst was constructed by anchoring Ni-N_4 and W-N_4 dual-atom sites on polymeric carbon nitride (CN) nanosheets via a wet chemical method followed by H_2/Ar atmosphere calcination. Atomic W sites served as superior centers for CO_2 adsorption and activation by the interacting with CO_2 via 5d orbital donation into π* antibonding orbitals [138]. Ni modified HOMO composition and accelerated charge separation. The optimized catalyst achieved CO formation rates of 80.4 μmol·g^{-1}·h^{-1}, 10.5 times higher than pristine

CN. Adjacent Co-Ag dual-metal sites coupled with Ag nanoparticles on P-doped g-C_3N_4 ($Co_1Ag_{(1+n)}$-PCN) were prepared [139]. The catalyst was obtained by a one-step solvothermal phosphidation of a pre-made Ag_1-CN with $CoCl_2$ and $NaH_2PO_2{\cdot}H_2O$, which generated Co-N_6-P entities and concurrently induced partial aggregation of Ag into nanoparticles while retaining Ag-N_2C_2 single-atom sites. *In situ* XPS verified electron flow from CN to Ag species through Co-N_6-P bridges. In a CH_3CN/H_2O (6:4) solid-liquid system without sacrificial agents, CO formation reached 11.7 μmol·g^{-1}·h^{-1} with 70.1% selectivity, outperforming Ag_1-CN and Co_1Ag_1-PCN. *In situ* FTIR detected CO_2* and COOH* intermediates, indicating a COOH*-mediated CO pathway, while the dual sites acted as fast electron-transfer channels and Ag nanoparticles served as electron sinks to promote product formation. La-Ni dual sites in a COF were prepared via electrostatically driven self-assembly (Fig. 13(a)) [135]. The La site functioned as an optically active center to broaden absorption (bandgap reduced to 2.86 eV) and promote charge generation, while the adjacent Ni site selectively catalyzed CO_2-to-CO conversion through a *COOH-mediated pathway (Fig. 13(b)). Directional electron transfer from La to Ni suppressed recombination and lowered the *COOH barrier, enabling a high CO evolution rate of 605.8 μmol·g^{-1}·h^{-1} with 98.2% selectivity under UV-vis irradiation. To address sluggish sacrificial-agent-free CO_2 methanation, Co-In dual single atoms were engineered on g-C_3N_4 via an assembly-pyrolysis strategy using NH_2-MIL-68(In) as precursor [140]. XAFS confirmed isolated Co-N_4 and In-N_5 motifs (~5.8 Å), enabling synergistic charge redistribution and improved CO_2 adsorption. The optimized Co_1In_1/CN exhibited suppressed PL and an extended carrier lifetime of 10.9 ns. Under UV-vis irradiation in pure water, it achieved CH_4 and CO rates of 18.8 and 5.1 μmol·g^{-1}·h^{-1} with 79% CH_4 selectivity and no H_2 evolution.

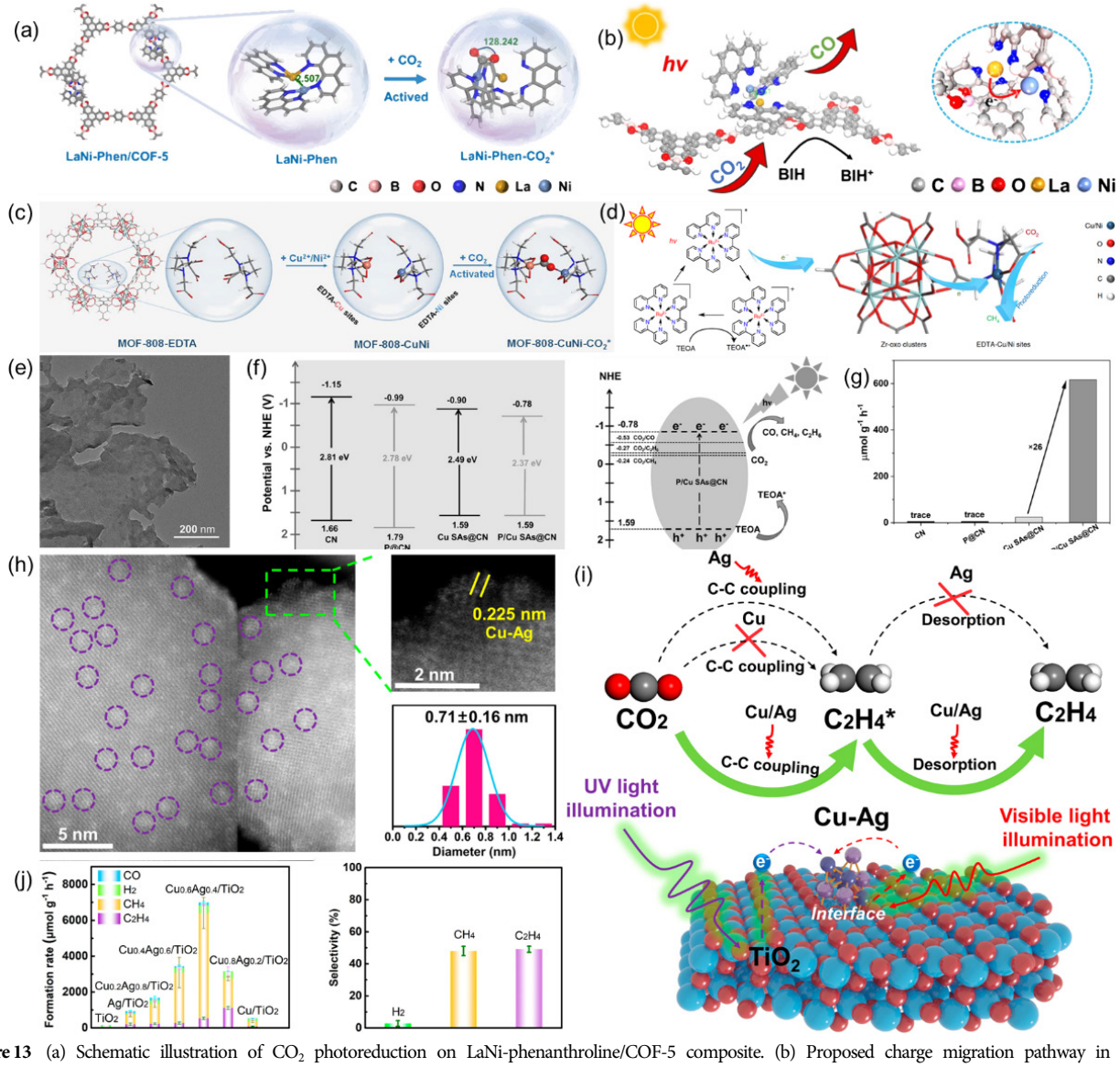

Figure 13 (a) Schematic illustration of CO_2 photoreduction on LaNi-phenanthroline/COF-5 composite. (b) Proposed charge migration pathway in LaNi-phenanthroline/COF-5 composite for CO_2 photoreduction. (a, b) Reprinted with permission from Ref. [135], © 2023 Zhou, D. et al. (c) Bioinspired CO_2 photoreduction over MOF-808-CuNi. (d) Proposed charge transfer mechanism over MOF-808-CuNi with $[Ru(bpy)_3]Cl_2{\cdot}6H_2O$ under visible light. (c, d) Reprinted with permission from Ref. [136], © Li, J. et al. under exclusive licence to Springer Nature Limited 2021, corrected publication 2022. (e) TEM image of P/Cu SAs@CN. (f) Band alignment of P/Cu SAs@CN. (g) Comparative C_2H_6 evolution from CO_2 photoreduction. (e–g) Reprinted with permission from Ref. [137], © 2022 Wiley-VCH GmbH. (h) HAADF-STEM image of Cu-Ag ASNCs/TiO_2 and the size of Cu-Ag ASNCs. (i) Proposed photocatalytic conversion pathway on Cu-Ag ASNCs/TiO_2 for CO_2 reduction. (j) Evaluation of photocatalytic performance and selectivity on Cu-Ag ASNCs/TiO_2. (h–j) Reprinted with permission from Ref. [75], © 2023 Yu, Y. Y. et al. Published by PNAS.

DFT and DRIFTS revealed stabilization of *CHO intermediates, lowering the barrier from *COOH→*CO→*CHO and promoting deep hydrogenation toward methane. Flexible Cu-Ni dual-metal-site pairs (MOF-808-CuNi) were constructed by chelating Cu^{2+}/Ni^{2+} with EDTA and anchoring them into MOF-808 (Fig. 13(c)) [136], enabling dynamic, enzyme-like site adaptation. The MOF ensured light harvesting and CO_2 uptake, while photogenerated electrons migrated from the photosensitizer to Zr-oxo clusters and then to Cu-Ni sites, promoting a COOH*→CH_4 pathway (Fig. 13(d)). As a result, MOF-808-CuNi achieved a CH_4 rate of 158.7 μmol·g^{-1}·h^{-1} with ~99.4% electron selectivity under visible light.

To address the high kinetic barriers of C-C coupling in CO_2 photoreduction, this work constructed Au-Cu dual-atom sites on oxygen-defective Bi_2WO_6 (ACBT-O) via solvothermal synthesis followed by anaerobic photodeposition [141]. Au atoms occupied oxygen vacancies and accumulated electrons, while Cu atoms stabilized *CO intermediates, forming spatially isolated yet cooperative dual sites. The optimized $Au_{0.2}Cu_{0.3}$ sample achieved 83.9 μmol·g^{-1}·h^{-1} total yield with 65.4% C_{2+} selectivity under 2.4 W·cm^{-2} irradiation. DFT showed the C-C coupling barrier decreased to 0.363 eV on dual sites, far lower than single-atom counterparts (1.368 eV). *In situ* DRIFTS confirmed *COCO intermediates, indicating that Au-Cu synergy promoted multicarbon pathways through enhanced charge delocalization and intermediate stabilization. Moreover, atomically dispersed P-N and Cu-N_4 dual sites were constructed on carbon nitride nanosheets (P/Cu SAs@CN) via controlled heteroatom incorporation for light-driven CO_2 reduction to multicarbon products (Fig. 13(e)) [137]. P atoms replaced C sites to act as hole-capture centers, while Cu single atoms served as electron-accumulation sites (Fig. 13(f)), spatially separating carriers and prolonging lifetime to 7.13 ns. The bandgap narrowed to 2.37 eV, enhancing visible absorption. Under light irradiation in a gas-circulation reactor, the catalyst delivered a C_2H_6 evolution rate of 616.6 μmol·g^{-1}·h^{-1} with 33.0% selectivity and an AQE of 12.55% at 350 nm (Fig. 13(g)), 26 times higher than Cu-only samples. DFT and *in situ* FTIR identified *OC-COH intermediates with a moderate 0.45 eV barrier, confirming facilitated C-C coupling on charge-enriched Cu sites. Cu-Ag alloy sub-nanoclusters (ASNCs) were constructed as alloy sub-nanoclusters (~0.71 nm) on TiO_2 (Cu-Ag ASNCs/TiO_2) for efficient C-C coupling and facile C_2H_4 desorption in photocatalytic CO_2 reduction via a stepwise photodeposition route (Fig. 13(h)) [75]. The design ensured intimate atomic-level interaction and precise site exposure. The Cu-Ag alloy created strong interface states with TiO_2, enabling visible-light-driven hot-electron generation and rapid electron migration from TiO_2 to Cu-dominated active sites. Ag promoted CH_2*-CH_2* coupling, while Cu facilitated C_2H_4* desorption, synergistically steering the reaction pathway toward C_2H_4 (Fig. 13(i)). *In situ* FTIR and DFT revealed a lowered barrier for C-C coupling and moderated adsorption strength of C_2H_4*. Under simulated sunlight irradiation in pure CO_2/H_2O, the optimized $Cu_{0.8}Ag_{0.2}$/TiO_2 delivered a record C_2H_4 rate of 1110.6 μmol·g^{-1}·h^{-1} with 49.1% selectivity (Fig. 13(j)) and a quantum efficiency of 0.26%. Precisely distributed Cu-Ti dual-metal pairs were fabricated by anchoring Cu single atoms onto oxygen-vacancy-rich MIL-125(Ti)-NH_2 via calcination and impregnation, yielding well-defined Cu-Ti coordination [142]. Structurally, the vacancy-engineered MOF enhanced light absorption and facilitated strong metal-support interaction. Upon illumination, photogenerated electrons rapidly transferred from Ti to adjacent Cu, suppressing recombination and enabling excited-state structural self-regulation. Cu-Ti pairs stabilized *CHOCO intermediates through d-p hybridization, making C-C coupling thermodynamically spontaneous. Under simulated sunlight irradiation using CO_2 and H_2O without sacrificial agents, the catalyst achieved a solar-to-chemical efficiency of 0.62% with 78.3% electron selectivity toward C_2H_4, outperforming vacancy-free counterparts. Across these studies, CO_2 reduction followed a sequential pathway: CO_2→*COOH→*CO→further protonation or C-C coupling. In DACs, one site normally activated CO_2 or stabilized *COOH, while the second facilitated electron transfer or hydrogenation. Multicarbon production required adjacent adsorption of two *CO intermediates, enabled by geometric proximity of dual centers.

Dual-atom interfaces offer well-defined adjacent active sites, tunable electronic coupling, and synergistic pathways for multi-electron reactions [143–145], making them highly effective for H_2 evolution and selective CO_2 reduction. Their main limitations are complex synthesis, possible atom migration, and low structural stability under reaction conditions. They are most effective when precise atomic coordination and strong support interactions are achieved. The scalable synthesis, long-term durability, accurate structural identification, and understanding dynamic structure-activity relationships under *operando* conditions are still challenging.

4.5 A-B-A-B copolymer-like interfaces

A-B-A-B type copolymer-analogue structure was engineered by periodically stacking dissimilar phases or compositions to induce robust internal electric fields [122, 146–148]. These coherent interfaces effectively regulated carrier distributions, prolonging exciton lifetimes and suppressing bulk recombination to achieve ultrafast charge separation for efficient photocatalysis [149, 150]. Dipole moments usually possess alternately arranged atomic layers or repeating units and were collectively explored engineering to enhance photocatalytic efficiency. A macroscopic spontaneous polarization field in CdS single-crystal nanorods was strategically engineered by promoting oriented growth along the [0001] polar axis (Figs. 14(a) and 14(b)) [146]. This structural design vectorially superimposed polar units, yielding a 20.1-fold enhancement in the internal electric field intensity compared to isotropic nanoparticles. This robust driving force propelled bulk charge separation with an efficiency of 72.4% (an 80.4-fold increase) and simultaneously modulated the chemical state of anchored Pt single atoms by increasing their onsite electron density. Consequently, the highly polarized catalyst achieved an exceptional H_2 space-time yield of 118.5 mmol·g^{-1}·h^{-1} with an apparent quantum efficiency (AQE) of 57.7% at 420 nm. The induction of dipole moments by breaking long-range atomic order was explored in amorphous ZnCdS (AZCS). Theoretical calculations revealed that the asymmetric arrangement of ZnS_4 and CdS_4 tetrahedrons generated significant dipole moments [151], specifically reaching 197.01 eÅ along the *z*-direction, which was substantially higher than the symmetric crystalline counterpart. These induced dipole fields facilitated rapid directional charge transfer and broadened the light absorption range by reducing the bandgap to 2.34 eV. When loaded with Co-MoS_x cocatalysts, the amorphous system delivered a superior H_2 evolution rate of 70.13 mmol·g^{-1}·h^{-1}, outperforming the crystalline version by over five times while maintaining stability for 160 h. Integrating a bulk polarization electric field (PEF) from asymmetric $Zn_3In_4S_9$ with an interface dipole field (IDF) induced by MoS_2 was developed for photocatalytic H_2 evolution (Fig. 14(c)) [147]. The intrinsic dipole

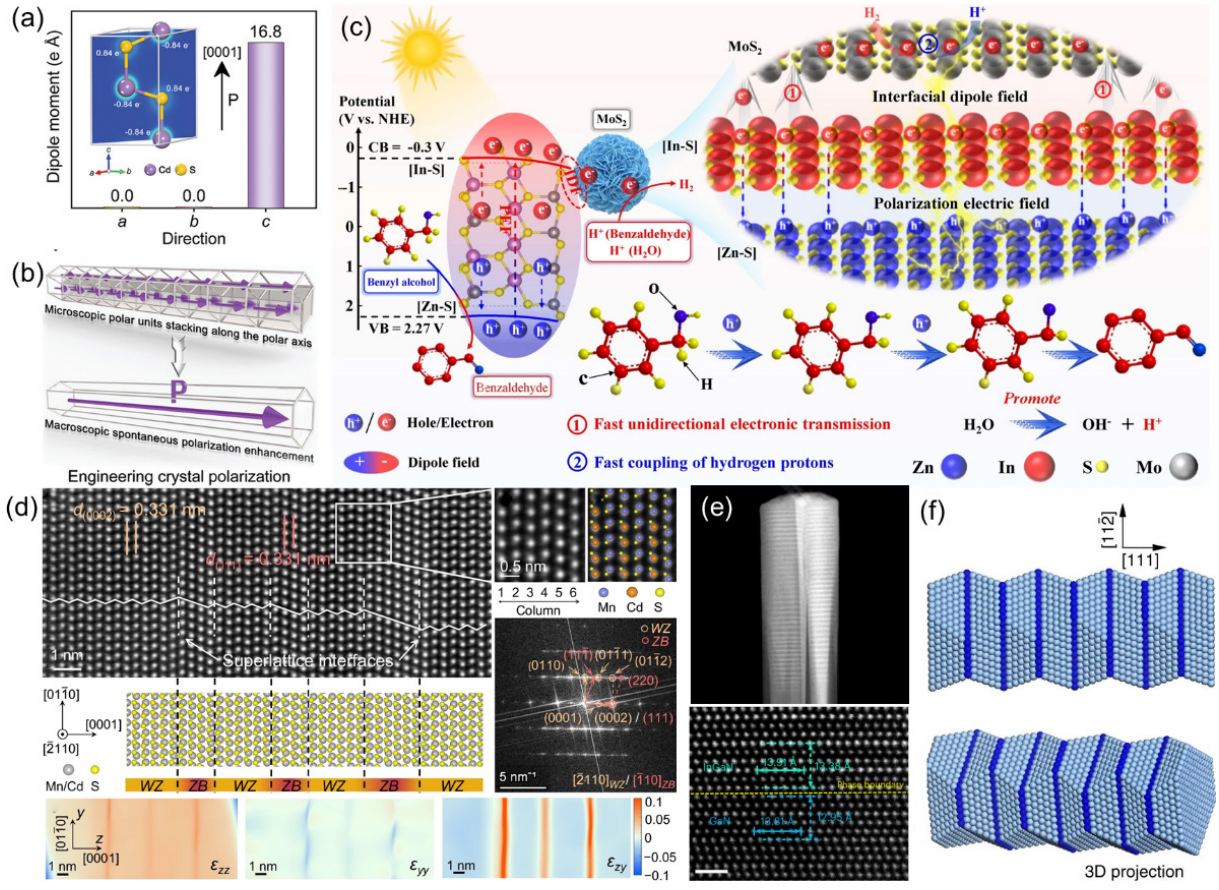

Figure 14 (a) Crystallographic orientation-dependent dipole moments in hexagonal CdS primary cell. (b) Polar unit alignment along *c*-axis inducing macroscopic polarization in CdS nanorod. (a, b) Reprinted with permission from Ref. [146], © 2024 Wiley-VCH GmbH. (c) Proposed dipole-field mechanism enabling H_2 generation and chemical conversion over $MoS_2/Zn_3In_4S_9$. Reprinted with permission from Ref. [147], © 2025 Wang, Z. N. et al. (d) One-dimensional axial superlattice $Mn_{0.5}Cd_{0.5}S$ nanorods with zinc blende/wurtzite phase-transition interfaces. Reprinted with permission from Ref. [148], © 2024 Wang, S. J. et al. (e) HAADF-STEM image of the InGaN/GaN interface region. Reprinted with permission from Ref. [11], © Pan, Y. Y. et al. under exclusive licence to Springer Nature Limited 2026, modified publication 2026. (f) Structural models of a typical twin nanocrystal as seen from the [$\bar{1}$10] direction. Reprinted with permission from Ref. [149], © 2013 Macmillan Publishers Limited.

of $Zn_3In_4S_9$ produced a potential difference of 2.51 eV and a dipole moment of 2.95 eÅ, while the MoS_2 modification created a massive potential difference of 9.63 eV at the interface. This synergy established a fast electron "highway" from $Zn_3In_4S_9$ to MoS_2, achieving H_2 and benzaldehyde production rates of 41.19 and 43.33 mmol·g^{-1}·h^{-1}, respectively. These values represented a 12-fold improvement over pristine materials, supported by a high AQE of 36.6% for hydrogen evolution.

Superlattice interfaces with periodic lattice stacking were developed to create robust internal electric fields. These architectures effectively suppressed charge recombination and prolonged carrier lifetimes, significantly accelerating solar-to-hydrogen conversion. Typically, one-dimensional axial superlattice $Mn_{0.5}Cd_{0.5}$ nanorods (SL-MCS NRs) featuring phase-transition-induced zinc blende/wurtzite superlattice interfaces were developed via ion exchange (Fig. 14(d)) [148]. These coherent homointerfaces were designed to create periodic internal electric fields that redistributed photoinduced carriers along the [0001] direction. By suppressing bulk recombination, this architecture, combined with S-scheme $MnWO_4$ nanoparticles, achieved a H_2 evolution rate of 54.4 mmol·g^{-1}·h^{-1} without cocatalysts-a fivefold increase over control samples-and an apparent quantum efficiency (AQE) of 63.1% at 420 nm. A sequential cation-exchange strategy was employed to construct sophisticated multicomponent nanostructures with atomically precise interfaces. By leveraging thermodynamic solubility differences and coordination equilibria, this versatile approach transformed simple templates into complex architectures like multi-node type-II ZnS-(CdS/metal) sheath nanorods [64] or noble-metal-free Janus-like g-MnS/Cu_7S_4 [152] structures. These engineered interfaces facilitated efficient charge steering and broadband light harvesting, significantly boosting photocatalytic H_2 evolution. The excitonic quantum superlattices composed of nanometer-scale InGaN/GaN layers were also explored (Fig. 14(e)) [11]. By precisely tuning superlattice dimensions (the optimal number of InGaN layers was determined to be 40), the researchers exploited the quantum-confined Stark effect (QCSE) and built-in piezoelectric fields (up to 0.9 MV·cm^{-1}) to prolong the lifetime of indirect excitons. This carrier-steering design facilitated surface reactions, resulting in a remarkable external quantum efficiency (EQE) of 95% at 365 nm and a solar-to-hydrogen (STH) efficiency of 3.16% under concentrated sunlight. One-dimensional $Cd_{0.5}Zn_{0.5}S$ nanorods were engineered to feature high-density, long-range ordered twinning superlattices [149]. These coherent twin boundaries induced numerous zinc-blende (ZB) and wurtzite (WZ) homojunctions along <111> direction with type-II staggered band alignment (Fig. 14(f)), which significantly accelerated vectorial charge transfer and yielded a remarkable 62% quantum efficiency for solar hydrogen evolution.

The copolymer-like interfaces offer periodically ordered

heterointerfaces, well-defined charge transport pathways, and strong electronic coupling, which are beneficial for efficient carrier separation and directional transfer. They are most effective in systems requiring precise spatial regulation of redox sites. However, their synthesis is often complex and highly sensitive to structural uniformity [153, 154]. The scalable fabrication, long-range structural stability, and understanding how periodic interfaces govern reaction pathways and selectivity are still challenging.

5 Summary and outlook

Atomic-scale interface engineering has reshaped photocatalytic research by shifting design principles from bulk band alignment to interfacial electronic precision. Despite remarkable progress, translating atomic-level insights into robust, scalable, and reaction-specific photocatalysts remains a central challenge for future solar-to-chemical conversion technologies.

First, future progress will rely on the rational construction of deterministic interfaces with well-defined bonding motifs and coordination environments. Moving beyond random heterojunction contact, precisely bridged atomic ensembles and epitaxial interfaces can establish predictable charge-transfer pathways and built-in electric fields, enabling directional carrier migration while preserving strong redox potentials. Achieving such control across different material classes remains a central challenge. Artificial intelligence (AI) enables data-driven discovery of atomic-scale interfaces by correlating structure-property relationships, accelerating predictive design, and guiding targeted synthesis.

Second, synthetic methodology innovation will be decisive. Advanced routes such as seed-mediated growth, cation exchange, and coordination-confined single/dual-atom anchoring offer scalable ways to integrate atomic precision with structural complexity. Future efforts should focus on expanding these strategies to non-ideal lattices and multicomponent systems while maintaining interfacial coherence and long-term stability.

Third, *operando* and ultrafast characterization must be further integrated with theory. Real-time probes capable of resolving interfacial charge dynamics, reconstruction, and intermediate evolution are essential to distinguish structure-function relationships at working conditions. Coupling these insights with predictive DFT and data-driven modeling will accelerate rational interface design.

Finally, emerging concepts such as superlattice architectures and dipole-engineered interfaces open new opportunities to manipulate internal electric fields at multiple length scales. By synergistically combining atomic precision with mesoscale ordering, photocatalysts can achieve higher quantum efficiency, improved selectivity, and better durability. Overall, atomic-scale interface engineering is poised to guide the next generation of photocatalytic systems toward practical and efficient solar fuel production.

Acknowledgements

The work was supported by the National Natural Science Foundation of China (92477134) and Provincial Natural Science Foundation of Shandong (ZR2023ME014).

Declaration of conflicting interests

The authors declare no conflicting interests regarding the content of this article.

Data availability

All data needed to support the conclusions in the paper are presented in the manuscript and/or the Supplementary Materials. Additional data related to this paper may be requested from the corresponding author upon request.

References

[1] Peng, M.; Li, C. Y.; Wang, Z. H.; Wang, M. L.; Zhang, Q. X.; Xu, B. J.; Li, M. F.; Ma, D. Interfacial catalysis at atomic level. *Chem. Rev.* **2025**, *125*, 2371–2439.

[2] Zhang, L. Y.; Zhang, J. J.; Yu, J. G.; García, H. Charge-transfer dynamics in S-scheme photocatalyst. *Nat. Rev. Chem.* **2025**, *9*, 328–342.

[3] Kosco, J.; Gonzalez-Carrero, S.; Howells, C. T.; Fei, T.; Dong, Y. F.; Sougrat, R.; Harrison, G. T.; Firdaus, Y.; Sheelamanthula, R.; Purushothaman, B. et al. Generation of long-lived charges in organic semiconductor heterojunction nanoparticles for efficient photocatalytic hydrogen evolution. *Nat. Energy* **2022**, *7*, 340–351.

[4] Yang, M. M.; Luo, Z. D.; Mi, Z.; Zhao, J. J.; E, S. P.; Alexe, M. Piezoelectric and pyroelectric effects induced by interface polar symmetry. *Nature* **2020**, *584*, 377–381.

[5] Deng, A. X.; Sun, Y.; Gao, Z. Q.; Yang, S. G.; Liu, Y. Z.; He, H.; Zhang, J. Q.; Liu, S. M.; Sun, H. Q.; Wang, S. B. Internal electric field in carbon nitride-based heterojunctions for photocatalysis. *Nano Energy* **2023**, *108*, 108228.

[6] Chu, X. Y.; Liu, S. K.; Luan, B. B.; Zhang, Y.; Xi, Y. M.; Shao, L. H.; Zhang, F. M.; Lan, Y. Q. Crystal-facet-controlled internal electric field in MOF/COF heterojunction towards efficient photocatalytic overall water splitting. *Angew. Chem., Int. Ed.* **2025**, *64*, e202422940.

[7] Yu, Z. Z.; Yang, K.; Yu, C. L.; Lu, K. Q.; Huang, W. Y.; Xu, L.; Zou, L. X.; Wang, S. B.; Chen, Z.; Hu, J. et al. Steering unit cell dipole and internal electric field by highly dispersed Er atoms embedded into NiO for efficient CO_2 photoreduction. *Adv. Funct. Mater.* **2022**, *32*, 2111999.

[8] Chen, K.; Cai, A. Q.; Li, T. T. Covalent organic framework-semiconductor-based heterostructures for photocatalytic applications. *ChemSusChem* **2023**, *16*, e202300021.

[9] Wang, Y.; Wang, D. S.; Li, Y. D. Atom-level interfacial synergy of single-atom site catalysts for electrocatalysis. *J. Energy Chem.* **2022**, *65*, 103–115.

[10] Zhou, S. L.; Li, H. J.; Gao, H. Y.; Li, A.; Li, T.; Cheng, S. S.; Wang, J. J.; Kasemchainan, J.; Yi, J. H.; Zhao, F. Q. et al. Recent advances in metal-loaded MOFs photocatalysts: From single atom, cluster to nanoparticle. *Chin. Chem. Lett.* **2025**, *36*, 110142.

[11] Pan, Y. Y.; Zhang, B. X.; Ye, Z. W.; Shen, Y. F.; Hanish, J.; Wu, Y. P.; Malhotra, Y.; Li, K. J.; Norris, T. B.; Mi, Z. T. Excitonic quantum superlattices for efficient photocatalytic water splitting. *Nat. Energy* **2026**, *11*, 571–580.

[12] Cai, B.; Brnovic, A.; Pavliuk, M. V.; Hammarström, L.; Kloo, L.; Barnett, S. A.; Tian, H. N. Organic crystalline nanoparticles with a long-lived charge-separated state for efficient photocatalytic hydrogen production. *Nat. Chem.* **2026**, *18*, 723–730.

[13] Liu, K. Y.; Wang, L. P.; Chen, W. X.; Sun, Z. Y.; Geng, H. L.; Li, Y. Q.; Deng, Z. W.; Jiang, S.; Zhou, B. R.; Yu, K. D. et al. The roadmap of carbon-based single-atom catalysts: Rational design and electrochemical applications. *Rare Met.* **2025**, *44*, 7987–8132.

[14] Li, W. L.; Liu, Z. Y.; Rhimi, B.; Zhou, M.; Li, J.; Nie, K. Q.; Yan, B. H.; Jiang, Z. F.; Shi, W. D.; Xiong, Y. J. Nitrogen-bridged S–N–Cu sites for CO_2 photoreduction to ethanol with 99.5% selectivity in pure water. *Angew. Chem., Int. Ed.* **2025**, *64*, e202423859.

[15] Hu, J. D.; Li, B. R.; Li, X.; Yang, T. Y.; Yang, X. G.; Qu, J. F.; Cai, Y. H.; Yang, H. B.; Lin, Z. Q. Lattice match-enabled covalent

heterointerfaces with built-in electric field for efficient hydrogen peroxide photosynthesis. *Adv. Mater.* **2024**, *36*, 2412070.
[16] Shao, Z. W.; Ye, C. C.; Zhang, Y.; Wu, Y.; Xiong, J.; Li, M. M. J.; Jiang, W.; Di, J. Epitaxial active interface to construct intralattice-bonded asymmetric Bi_1–O–Bi_2 sites for robust CO_2 photoreduction to acetic acid. *Angew. Chem., Int. Ed.* **2026**, *65*, e24970.
[17] Li, W.; Wang, E. Y.; Wang, H. Q.; Yang, Y.; Hu, S. X.; Liu, H. Construction of S-scheme heterostructure via anion and cation vacancy mediated electrostatically driven self-assembly in $Cd_{1-x}S$-CdS_{1-x} for robust photocatalytic CO_2 reduction. *Nano Energy* **2025**, *142*, 111235.
[18] Cao, Y. H.; Guo, L.; Dan, M.; Doronkin, D. E.; Han, C. Q.; Rao, Z. Q.; Liu, Y.; Meng, J.; Huang, Z. A.; Zheng, K. B. et al. Modulating electron density of vacancy site by single Au atom for effective CO_2 photoreduction. *Nat. Commun.* **2021**, *12*, 1675.
[19] Zhang, H.; Chen, L.; Dong, F.; Lu, Z. W.; Lv, E. M.; Dong, X. L.; Li, H. X.; Yuan, Z. Y.; Peng, X. W.; Yang, S. H. et al. Dynamic transformation of active sites in energy and environmental catalysis. *Energy Environ. Sci.* **2024**, *17*, 6435–6481.
[20] Stanley, P. M.; Ramm, V.; Fischer, R. A.; Warnan, J. Analysis of metal-organic framework-based photosynthetic CO_2 reduction. *Nat. Synth.* **2024**, *3*, 307–318.
[21] Xue, Z. H.; Luan, D. Y.; Zhang, H. B.; Lou, X. W. Single-atom catalysts for photocatalytic energy conversion. *Joule* **2022**, *6*, 92–133.
[22] Xue, Z. G.; Gao, X. P.; Zhang, Y. D.; Yan, M. Y.; Xu, J. Q.; Wu, Y. E. Site-coverage dependent single-atom-layer catalysts toward hydrogen production. *Chem Catal.* **2023**, *3*, 100538.
[23] Gao, Z. Y.; Montini, T.; Mu, J. J.; Luo, N. C.; Fonda, E.; Fornasiero, P.; Wang, F. Photocatalytic methanol dehydrogenation promoted synergistically by atomically dispersed Pd and clustered Pd. *J. Am. Chem. Soc.* **2024**, *146*, 24440–24449.
[24] Bonchio, M.; Bonin, J.; Ishitani, O.; Lu, T. B.; Morikawa, T.; Morris, A. J.; Reisner, E.; Sarkar, D.; Toma, F. M.; Robert, M. Best practices for experiments and reporting in photocatalytic CO_2 reduction. *Nat. Catal.* **2023**, *6*, 657–665.
[25] Liu, X. B.; Zhuang, H. Q. Recent progresses in photocatalytic hydrogen production: Design and construction of Ni-based cocatalysts. *Int. J. Energy Res.* **2021**, *45*, 1480–1495.
[26] Kudo, A.; Miseki, Y. Heterogeneous photocatalyst materials for water splitting. *Chem. Soc. Rev.* **2009**, *38*, 253–278.
[27] Ma, M. J.; Wang, H. Q.; Liu, H. Steering spatially separated dual sites on nano-TiO_2 through SMSI and lattice matching for robust photocatalytic hydrogen evolution. *Chin. Chem. Lett.* **2021**, *32*, 3613–3618.
[28] Zhang, J.; Hu, Z. W.; Zheng, J. L.; Xiao, Y. Q.; Song, J.; Li, X. T.; Cheng, C. X.; Zhang, Z. Y. Photothermal-assisted solar hydrogen production: A review. *Energy Convers. Manage.* **2024**, *318*, 118901.
[29] Qiao, F. Photoelectrocatalytic hydrogen production: Hydrogen production principle, performance optimization strategy, application and prospect. *Nano Res. Energy* **2025**, *4*, e9120132.
[30] Wong, K. J.; Foo, J. J.; Siang, T. J.; Ong, W. J. Transition metal carbide-based photocatalysts for artificial photosynthesis. *SmartMat* **2024**, *5*, e1238.
[31] Jia, G. R.; Zhang, Y. C.; Yu, J. C.; Guo, Z. X. Asymmetric atomic dual-sites for photocatalytic CO_2 reduction. *Adv. Mater.* **2024**, *36*, 2403153.
[32] Wang, Y. O.; Chen, E. Q.; Tang, J. W. Insight on reaction pathways of photocatalytic CO_2 conversion. *ACS Catal.* **2022**, *12*, 7300–7316.
[33] Wang, P.; Wang, L. M.; Liu, L. P.; Lin, Z. X.; Zhao, Z. Y.; Gao, H. Y.; Zhang, L. G.; Zhang, X. W.; Wang, G.; Irvine, J. T. S. Regulation of *d*-band centers in layered double hydroxide nanocages through Zn doping for improved photocatalytic CO_2 reduction. *Nano Res. Energy* **2025**, *4*, e9120191.
[34] Ortiz-Quiñonez, J. L.; Pal, U. Interface engineered metal oxide heterojunction nanostructures in photocatalytic CO_2 reduction: Progress and prospects. *Coord. Chem. Rev.* **2024**, *516*, 215967.
[35] Zhang, A.; Cai, Y. M.; Guo, L.; Wang, C.; Wa, Q.; Xu, Y. P.; Zhou, J.; Fan, H. S.; Li, Z. Y.; Long, X. Y. et al. Recent progress in CO_2 conversion: An overview of catalytic strategies for sustainable fuel and chemical synthesis. *SmartMat* **2025**, *6*, e70058.
[36] Shen, J.; Wang, D. S. How to select heterogeneous CO_2 reduction electrocatalyst. *Nano Res. Energy* **2024**, *3*, e9120096.
[37] Qiu, N.; Li, J. J.; Wang, H. Q.; Zhang, Z. C. Emerging dual-atomic-site catalysts for electrocatalytic CO_2 reduction. *Sci. China Mater.* **2022**, *65*, 3302–3323.
[38] Qiu, N.; Lu, W.; Wang, H. Q. Manipulating local CO_2/H_2O ratio in electrocatalytic CO_2 reduction toward multi-carbon product. *Rare Met.* **2025**, *44*, 60–80.
[39] Wang, H. Q. Nanostructure@metal-organic frameworks (MOFs) for catalytic carbon dioxide (CO_2) conversion in photocatalysis, electrocatalysis, and thermal catalysis. *Nano Res.* **2022**, *15*, 2834–2854.
[40] Zhang, H. B.; Wang, C. J. Photothermal synergistic catalysis and associated kinetics. *China Powder Sci. Technol.* **2025**, *31*, 11–21.
[41] Zhou, W. J.; Wu, T.; Chen, Y. K.; Yu, W. Q.; Wang, Y. J.; Li, Y.; Yuan, H. F.; Liu, X. Y.; Wang, Y. J.; Kong, H. et al. Preparation of nanomaterials by laser and their application in new energy catalysis. *China Powder Sci. Technol.* **2025**, *31*, 71–90.
[42] Song, Y. H.; Zhao, H. R.; Lu, W.; Wang, H. Q. Unlocking hydrogen transfer pathway in electrocatalytic CO_2 reduction: Paving the way for precise selectivity control. *Nano Res.* **2025**, *18*, 94907384.
[43] Xia, Y. N.; Gilroy, K. D.; Peng, H. C.; Xia, X. H. Seed-mediated growth of colloidal metal nanocrystals. *Angew. Chem., Int. Ed.* **2017**, *56*, 60–95.
[44] He, M. Q.; Ai, Y. J.; Hu, W. T.; Guan, L. D.; Ding, M. Y.; Liang, Q. L. Recent advances of seed-mediated growth of metal nanoparticles: From growth to applications. *Adv. Mater.* **2023**, *35*, 2211915.
[45] Lozovoy, K. A.; Korotaev, A. G.; Kokhanenko, A. P.; Dirko, V. V.; Voitsekhovskii, A. V. Kinetics of epitaxial formation of nanostructures by Frank-van der Merwe, Volmer-Weber and Stranski-Krastanow growth modes. *Surf. Coat. Technol.* **2020**, *384*, 125289.
[46] Xu, B.; He, P. L.; Liu, H. L.; Wang, P. P.; Zhou, G.; Wang, X. A 1D/2D helical CdS/$ZnIn_2S_4$ nano-heterostructure. *Angew. Chem., Int. Ed.* **2014**, *53*, 2339–2343.
[47] Xu, B.; Li, H. Y.; Yang, H.; Xiang, W. T.; Zhou, G.; Wu, Y.; Wang, X. Colloidal 2D-0D lateral nanoheterostructures: A case study of site-selective growth of CdS nanodots onto Bi_2Se_3 nanosheets. *Nano Lett.* **2015**, *15*, 4200–4205.
[48] Zhong, Q. X.; Feng, J.; Jiang, B.; Fan, Y. L.; Zhang, Q.; Chen, J. X.; Yin, Y. D. Strain-modulated seeded growth of highly branched black Au superparticles for efficient photothermal conversion. *J. Am. Chem. Soc.* **2021**, *143*, 20513–20523.
[49] Xu, B.; Zhang, W. J.; Zhou, Z. H.; Lu, X. Q.; Li, J.; Pan, G. L.; Lou, Y. Research progress on thermoelectric metalorganic frameworks and covalent organic frameworks materials. *China Powder Sci. Technol.* **2025**, *31*, 61–73.
[50] Chen, J. X.; Feng, J.; Yang, F.; Aleisa, R.; Zhang, Q.; Yin, Y. D. Space-confined seeded growth of Cu nanorods with strong surface plasmon resonance for photothermal actuation. *Angew. Chem., Int. Ed.* **2019**, *58*, 9275–9281.
[51] Naya, S. I.; Kume, T.; Akashi, R.; Fujishima, M.; Tada, H. Red-light-driven water splitting by Au(core)-CdS(shell) half-cut nanoegg with heteroepitaxial junction. *J. Am. Chem. Soc.* **2018**, *140*, 1251–1254.
[52] Chen, J. Z.; Ma, Q. L.; Wu, X. J.; Li, L. X.; Liu, J. W.; Zhang, H. Wet-chemical synthesis and applications of semiconductor nanomaterial-based epitaxial heterostructures. *Nano-Micro Lett.* **2019**, *11*, 86.
[53] Jin, N.; Sun, Y. L.; Shi, W. W.; Wang, P.; Nagaoka, Y.; Cai, T.;

Wu, R. Z.; Dube, L.; Nyiera, H. N.; Liu, Y. Z. et al. Type-I CdS/ZnS core/shell quantum dot-gold heterostructural nanocrystals for enhanced photocatalytic hydrogen generation. *J. Am. Chem. Soc.* **2023**, *145*, 21886–21896.

[54] Hao, J. J.; Liu, H. C.; Duan, X. J.; Zhou, Z. M.; Zhao, B. X.; Zhang, W. D.; Xu, B.; Sun, X. W.; Delville, M. H. Shape control of CdSe/CdS nanocrystals during shell formation and growth: Dominating effects of surface ligands over core crystal structure. *Sci. China Mater.* **2023**, *66*, 3621–3628.

[55] Xu, X. Y.; Lu, Q. H.; Wu, J. W.; Mo, W.; Zuo, L.; Yang, N.; Xia, W. W.; Zeng, X. H. Boosting solar driven hydrogen production rate of Cu_2S@CdS p-n heterostructures and $Cu_xCd_{1-x}S$ nanorods. *Int. J. Hydrogen Energy* **2024**, *51*, 869–879.

[56] Wan, X. D.; Pan, Y.; Xu, Y. J.; Liu, J.; Chen, H. L.; Pan, R. R.; Zhao, Y. Z.; Su, P. W.; Li, Y. M.; Zhang, X. M. et al. Ultralong lifetime of plasmon-excited electrons realized in nonepitaxial/epitaxial Au@CdS/$CsPbBr_3$ triple-heteronanocrystals. *Adv. Mater.* **2023**, *35*, 2207555.

[57] Tian, J. Q.; Zhang, Y. Y.; Shi, Z. H.; Liu, Z. Y.; Zhao, Z. W.; Li, J.; Li, N.; Huang, H. W. Enabling interfacial lattice matching by selective epitaxial growth of CuS crystals on Bi_2WO_6 nanosheets for efficient CO_2 photoreduction into solar fuels. *Angew. Chem., Int. Ed.* **2025**, *64*, e202418496.

[58] Zhao, M. T.; Chen, J. Z.; Chen, B.; Zhang, X.; Shi, Z. Y.; Liu, Z. Q.; Ma, Q. L.; Peng, Y. W.; Tan, C. L.; Wu, X. J. et al. Selective epitaxial growth of oriented hierarchical metal-organic framework heterostructures. *J. Am. Chem. Soc.* **2020**, *142*, 8953–8961.

[59] Saruyama, M.; Sato, R.; Teranishi, T. Transformations of ionic nanocrystals via full and partial ion exchange reactions. *Acc. Chem. Res.* **2021**, *54*, 765–775.

[60] Beberwyck, B. J.; Surendranath, Y.; Alivisatos, A. P. Cation exchange: A versatile tool for nanomaterials synthesis. *J. Phys. Chem. C* **2013**, *117*, 19759–19770.

[61] Hou, H. L.; Bowen, C. R.; Yang, D. J.; Yang, W. Y. Cation-exchange-upgraded nanostructures for photocatalysts. *Chem* **2024**, *10*, 800–831.

[62] Robinson, R. D.; Sadtler, B.; Demchenko, D. O.; Erdonmez, C. K.; Wang, L. W.; Alivisatos, A. P. Spontaneous superlattice formation in nanorods through partial cation exchange. *Science* **2007**, *317*, 355–358.

[63] Liu, G. N.; Kolodziej, C.; Jin, R.; Qi, S. P.; Lou, Y. B.; Chen, J. X.; Jiang, D. C.; Zhao, Y. X.; Burda, C. MoS_2-stratified CdS-$Cu_{2-x}S$ core-shell nanorods for highly efficient photocatalytic hydrogen production. *ACS Nano* **2020**, *14*, 5468–5479.

[64] Zhuang, T. T.; Liu, Y.; Sun, M.; Jiang, S. L.; Zhang, M. W.; Wang, X. C.; Zhang, Q.; Jiang, J.; Yu, S. H. A unique ternary semiconductor-(semiconductor/metal) nano-architecture for efficient photocatalytic hydrogen evolution. *Angew. Chem., Int. Ed.* **2015**, *54*, 11495–11500.

[65] Que, L. X.; Lu, L.; Xu, Y. L.; Xu, X. Q.; Li, H.; Cao, J.; Zhu, M.; Li, C. R.; Pan, J. Q. The $ZnIn_2S_4$/CdS hollow core-shell nanoheterostructure towards enhanced visible light photocatalytic H_2 evolution via bimetallic synergism. *Int. J. Hydrogen Energy* **2023**, *48*, 4708–4718.

[66] Li, Y. X.; Li, S. Q.; Meng, L. H.; Peng, S. Q. Synthesis of oriented J type $ZnIn_2S_4$@$CdIn_2S_4$ heterojunction by controllable cation exchange for enhancing photocatalytic hydrogen evolution. *J. Colloid Interface Sci.* **2023**, *650*, 266–274.

[67] Wang, H. Z.; Gao, Y. Y.; Liu, J.; Li, X. Y.; Ji, M. W.; Zhang, E. H.; Cheng, X. Y.; Xu, M.; Liu, J. J.; Rong, H. P. et al. Efficient plasmonic Au/CdSe nanodumbbell for photoelectrochemical hydrogen generation beyond visible region. *Adv. Energy Mater.* **2019**, *9*, 1803889.

[68] Pan, Q.; Li, J.; Yan, L. G. Research progress of photothermal material-wood evaporators for solar-driven interfacial evaporation. *China Powder Sci. Technol.* **2024**, *30*, 90–102.

[69] Lei, H.; Zhang, J. P.; Wu, Z. Y.; Qi, W. Q.; Zhang, M. Y.; Li, Z. J.; Chen, L.; Hong, M. C. *In-situ* growth of $ZnIn_2S_4$ nanosheets on a Ti-based MOF to form a core-shell heterojunction for enhanced photocatalytic hydrogen evolution. *Sci. China Mater.*, in press, DOI: 10.1007/s40843-025-3875-1.

[70] Zhan, Z. H.; Wei, Z. H.; Zhang, Z. T.; Wang, L. P.; Cheong, W. C.; Li, S. H.; Chen, W. X.; Pang, S. P. Precisely designing atomically dispersed catalysts for C–N coupling reactions. *Nano Res. Energy* **2025**, *4*, e9120197.

[71] Zhang, W. Y.; Chao, Y. G.; Zhang, W. S.; Zhou, J. H.; Lv, F.; Wang, K.; Lin, F. X.; Luo, H.; Li, J.; Tong, M. P. et al. Emerging dual-atomic-site catalysts for efficient energy catalysis. *Adv. Mater.* **2021**, *33*, 2102576.

[72] Cheng, L.; Yue, X. Y.; Wang, L. X.; Zhang, D. N.; Zhang, P.; Fan, J. J.; Xiang, Q. J. Dual-single-atom tailoring with bifunctional integration for high-performance CO_2 photoreduction. *Adv. Mater.* **2021**, *33*, 2105135.

[73] Wang, Y.; Mao, J.; Meng, X. G.; Yu, L.; Deng, D. H.; Bao, X. H. Catalysis with two-dimensional materials confining single atoms: Concept, design, and applications. *Chem. Rev.* **2019**, *119*, 1806–1854.

[74] Li, S.; Guan, A. X.; Yang, C.; Peng, C.; Lv, X. M.; Ji, Y. L.; Quan, Y. L.; Wang, Q. H.; Zhang, L. J.; Zheng, G. F. Dual-atomic Cu sites for electrocatalytic CO reduction to C_{2+} products. *ACS Mater. Lett.* **2021**, *3*, 1729–1737.

[75] Yu, Y. Y.; He, Y.; Yan, P.; Wang, S. Y.; Dong, F. Boosted C–C coupling with Cu–Ag alloy sub-nanoclusters for CO_2-to-C_2H_4 photosynthesis. *Proc. Natl. Acad. Sci. USA* **2023**, *120*, e2307320120.

[76] Chen, L. Y.; Yang, S.; Yao, S. Y.; Si, Z. H.; Ding, G. C.; Zhan, P.; Song, J.; Cui, M.; Lu, L.; Qin, P. Y. Modulating adsorption configuration of intermediates on Cu–In dual-atom catalyst for boosted urea electrosynthesis. *Appl. Catal. B: Environ. Energy* **2025**, *379*, 125710.

[77] Pan, F. H. K.; Jin, T.; Yang, W. W.; Li, H.; Cao, Y. Q.; Hu, J.; Zhou, X. G.; Liu, H. L.; Duan, X. Z. Theory-guided design of atomic Fe–Ni dual sites in N, P-co-doped C for boosting oxygen evolution reaction. *Chem Catal.* **2021**, *1*, 734–745.

[78] Huang, J. R.; Chen, H. Y.; Zhu, H. L.; Liao, P. Q.; Chen, X. M. Ni–Zn dual-atom sites enable synergistic parallel pathways for efficient photosynthesis of H_2O_2 with long-term stability. *J. Am. Chem. Soc.* **2025**, *147*, 37167–37175.

[79] Dou, D. T.; Zhang, S. D.; Deng, J. J.; Wang, W. K.; Guan, X. H.; Zhou, T. S. Dual-atom cascade catalysis: *In situ* photogeneration and Lewis acid activation of H_2O_2 over Ag–Ga sites for antibiotic degradation. *Appl. Catal. B: Environ. Energy* **2026**, *388*, 126532.

[80] Tang, Y. H.; Zheng, Z. W.; Liu, H. M.; Wang, W.; Su, Z. Z.; Song, X. Y.; Zhou, Y. C.; Zhou, S. L.; Dong, Y. R.; Li, H. X. et al. Synergistic PtAg dual-atom sites boost photocatalytic nonoxidative methyl activation for coproduction of 1,2-diphenylethane and hydrogen from toluene. *Adv. Mater.* **2026**, *38*, e21903.

[81] Wei, T. C.; Ding, P. J.; Wang, T.; Liu, L. M.; An, X. Q.; Yu, X. L. Facet-regulating local coordination of dual-atom cocatalyzed TiO_2 for photocatalytic water splitting. *ACS Catal.* **2021**, *11*, 14669–14676.

[82] Li, Y. Z.; Li, Y. J.; Sun, H.; Gao, L. Y.; Jin, X. R.; Li, Y. P.; Lv, Z.; Xu, L. J.; Liu, W.; Sun, X. M. Current status and perspectives of dual-atom catalysts towards sustainable energy utilization. *Nano-Micro Lett.* **2024**, *16*, 139.

[83] Kim, J.; Baik, S. S.; Ryu, S. H.; Sohn, Y.; Park, S.; Park, B. G.; Denlinger, J.; Yi, Y.; Choi, H. J.; Kim, K. S. Observation of tunable band gap and anisotropic Dirac semimetal state in black phosphorus. *Science* **2015**, *349*, 723–726.

[84] Gou, W. K.; Sun, H. M.; Cheng, F. Y. Dual active sites engineering of electrocatalysts for alkaline hydrogen evolution. *Nano Res. Energy* **2024**, *3*, e9120121.

[85] Chen, J.; Xiao, Y. K.; Da, Y. M.; Chen, G. W.; Sun, Y. Y.; Wang, L.; Zhang, J.; Chen, W. Mechanistic insights and advances in electrode/electrolyte interfaces for efficient electrocatalytic CO_2

reduction to C_2 products. *SmartMat* **2025**, *6*, e1324.
[86] Song, Y. H.; Zhao, H. R.; Lu, W.; Wang, H. Q. Visualizing atom-scale surface restructuring of Cu-based electrocatalyst in electrocatalytic CO_2 reduction toward multicarbon product. *Rare Met.* **2025**, *44*, 4309–4311.
[87] Ma, W. C.; Xie, S. J.; Liu, T. T.; Fan, Q. Y.; Ye, J. Y.; Sun, F. F.; Jiang, Z.; Zhang, Q. H.; Cheng, J.; Wang, Y. Electrocatalytic reduction of CO_2 to ethylene and ethanol through hydrogen-assisted C–C coupling over fluorine-modified copper. *Nat. Catal.* **2020**, *3*, 478–487.
[88] Han, X.; Wang, H. Q.; Sun, C. H.; Xue, H. External-field-driven functional nanomaterials for interdisciplinary engineering-medicine applications. *SmartMat* **2025**, *6*, e70053.
[89] Wang, Q.; Pornrungroj, C.; Linley, S.; Reisner, E. Strategies to improve light utilization in solar fuel synthesis. *Nat. Energy* **2022**, *7*, 13–24.
[90] Bhattacharjee, S.; Linley, S.; Reisner, E. Solar reforming as an emerging technology for circular chemical industries. *Nat. Rev. Chem.* **2024**, *8*, 87–105.
[91] Wang, B.; Chen, H. L.; Huang, F. C.; Liu, J. Y.; Liu, G. P.; Weng, Y. X.; She, Y. B.; Zhu, X. W.; Li, H. M.; Xia, J. X. et al. Epitaxial $Bi_4O_5Br_2$ nanosheets on hollow carbon spheres for confined electron pump reactor and enhanced photocatalytic CO_2 hydrogenation reduction. *Appl. Catal. B: Environ. Energy* **2025**, *374*, 125394.
[92] Le Huec, T.; López-Francés, A.; Abánades Lázaro, I.; Navalón, S.; Baldoví, H. G.; Giménez-Marqués, M. Heteroepitaxial MOF-on-MOF photocatalyst for solar-driven water splitting. *ACS Nano* **2024**, *18*, 20201–20212.
[93] Das, R.; Patra, A.; Dutta, S. K.; Shyamal, S.; Pradhan, N. Facets-directed epitaxially grown lead halide perovskite-sulfobromide nanocrystal heterostructures and their improved photocatalytic activity. *J. Am. Chem. Soc.* **2022**, *144*, 18629–18641.
[94] Han, Y. W.; Zhang, Y. X.; Ye, L.; Gong, T. J.; Lu, X. B.; Yan, N.; Fu, Y. Establishing dual-interface built-in electric fields within Janus heterostructures for cooperative photoredox catalysis. *J. Am. Chem. Soc.* **2025**, *147*, 18637–18650.
[95] Li, L. F.; Li, Y. F.; Liu, Z. P. CO_2 photoreduction via quantum tunneling: Thin TiO_2-coated gap with coherent interface to achieve electron tunneling. *ACS Catal.* **2019**, *9*, 5668–5678.
[96] Chen, H.; Xiong, Y. Y.; Li, J.; Abed, J.; Wang, D.; Pedrazo-Tardajos, A.; Cao, Y. P.; Zhang, Y. T.; Wang, Y.; Shakouri, M. et al. Epitaxially grown silicon-based single-atom catalyst for visible-light-driven syngas production. *Nat. Commun.* **2023**, *14*, 1719.
[97] He, Z. L.; Zhang, J.; Li, X.; Guan, S. N.; Dai, M. C.; Wang, S. G. 1D/2D heterostructured photocatalysts: From design and unique properties to their environmental applications. *Small* **2020**, *16*, 2005051.
[98] Lin, H. F.; Kong, M. D.; Zou, Z. T.; Li, X.; Wang, H.; Xu, J. X.; Turkevich, V.; Li, Y. Y.; Wang, X.; Wang, L. Anisotropically epitaxial P–N heterostructures actuating efficient Z-scheme photocatalytic water splitting. *Small* **2025**, *21*, 2410751.
[99] Shi, X.; Dai, W. D.; Li, X. Q.; Zhu, Z. R.; Dong, X. A.; Cui, Z. H. Lattice-matched S-scheme high-entropy oxide heterojunction for efficient visible-light-driven CO_2 photomethanation. *Adv. Funct. Mater.* **2025**, *35*, e11696.
[100] Li, J.; Yu, X. M.; Xue, W. J.; Nie, L.; Huang, H. L.; Zhong, C. L. Engineering the direct Z-scheme systems over lattice intergrown of MOF-on-MOF for selective CO_2 photoreduction to CO. *AIChE J.* **2023**, *69*, e17906.
[101] Yuan, K.; Liu, Z. Y.; Yan, Z.; Yun, Q. B.; Song, T. Q.; Guo, J.; Zhang, X. T.; Zhong, D. C.; Tang, Z. Y.; Lu, T. B. et al. Metal-organic framework-based hetero-phase nanostructure photocatalysts with molecular-scale tunable energy levels. *Angew. Chem., Int. Ed.* **2024**, *63*, e202402693.
[102] Zhang, K.; Kim, J. K.; Park, B.; Qian, S. F.; Jin, B. J.; Sheng, X. W.; Zeng, H. B.; Shin, H.; Oh, S. H.; Lee, C. L. et al. Defect-induced epitaxial growth for efficient solar hydrogen production. *Nano Lett.* **2017**, *17*, 6676–6683.
[103] Zhang, J. Q.; Li, Y. G.; Zhao, X. L.; Zhang, H. Y.; Wang, L.; Chen, H. J.; Wang, S. J.; Xu, X. Y.; Shi, L.; Zhang, L. C. et al. A hydrogen-initiated chemical epitaxial growth strategy for in-plane heterostructured photocatalyst. *ACS Nano* **2020**, *14*, 17505–17514.
[104] Cheng, J. Z.; Cheng, B.; Xu, J. S.; Yu, J. G.; Cao, S. W. Organic-inorganic S-scheme heterojunction photocatalysts: Design, synthesis, applications, and challenges. *eScience* **2025**, *5*, 100354.
[105] Sun, B. J.; Huang, C.; Yang, C. Y.; Ke, D.; Liu, Y.; Lu, Q.; Liu, X. F.; Xiong, X. Y.; Chen, Y. Z.; Jiang, Q. Q. et al. Atomic interfacial charge and energy transfer paths at MoS_2/Pd bonded defect-rich BiOCl interfaces for efficient photocatalysis. *Appl. Catal. B: Environ. Energy* **2024**, *345*, 123720.
[106] Zhong, F. Y.; Sheng, J. P.; Du, C. Y.; He, Y.; Zhang, F. Y.; Sun, Y. J.; Zhou, Y.; Dong, F. Co-atomic interface minimizing charge transfer barrier in polytypic perovskites for CO_2 photoreduction. *Adv. Sci.* **2025**, *12*, 2410437.
[107] Che, Y.; Weng, B.; Li, K. J.; He, Z. L.; Chen, S. F.; Meng, S. G. Chemically bonded nonmetallic LSPR S-scheme hollow heterostructure for boosting photocatalytic performance. *Appl. Catal. B: Environ. Energy* **2025**, *361*, 124656.
[108] Fang, J. J.; Wu, Y.; Hu, H. L.; Xu, H. M.; Zhu, A. N.; Chen, Y. K.; Zhu, X. W.; Mao, J. J. Interfacial Zn–O–Ti sites for efficient photocatalytic urea synthesis from CO_2 and N_2. *Angew. Chem., Int. Ed.* **2025**, *64*, e202517121.
[109] Zhong, W.; Wang, J. T.; Meng, A. Y.; He, B.; Han, P. G.; Su, Y. R. Ag-oriented p-orbital electron modulation of active S atoms in core-shell Ag@MoS_2 cocatalyst for efficient photocatalytic H_2 production. *Chem. Eng. J.* **2025**, *519*, 164921.
[110] He, B. W.; Xiao, P.; Wan, S. J.; Zhang, J. J.; Chen, T.; Zhang, L. Y.; Yu, J. G. Rapid charge transfer endowed by interfacial Ni–O bonding in S-scheme heterojunction for efficient photocatalytic H_2 and imine production. *Angew. Chem., Int. Ed.* **2023**, *62*, e202313172.
[111] Zhang, H. Y.; Yang, Y.; Li, C. C.; Tang, H. L.; Zhang, F. M.; Zhang, G. L.; Yan, H. A new strategy for constructing covalently connected MOF@COF core-shell heterostructures for enhanced photocatalytic hydrogen evolution. *J. Mater. Chem. A* **2021**, *9*, 16743–16750.
[112] Zhang, Y.; Guo, F. Y.; Di, J.; Wang, K. K.; Li, M. M. J.; Dai, J. Y.; She, Y. B.; Xia, J. X.; Li, H. M. Strain-induced surface interface dual polarization constructs PML-Cu/$Bi_{12}O_{17}Br_2$ high-density active sites for CO_2 photoreduction. *Nano-Micro Lett.* **2024**, *16*, 90.
[113] Yi, W. J.; Wei, S.; Du, X.; Yi, S. S.; Tian, Z. L.; Liu, Z. Y.; Yue, X. Z. Strong interfacial bonded $In_{4/3}P_2S_6$/TiO_2 S-scheme junction with multi-channel charge transport for boosting photocatalytic water reduction. *Nano Res.* **2025**, *18*, 94907423.
[114] Zhang, Q.; Zhang, J. H.; Wang, X. H.; Li, L. F.; Li, Y. F.; Dai, W. L. In–N–In sites boosting interfacial charge transfer in carbon-coated hollow tubular In_2O_3/$ZnIn_2S_4$ heterostructure derived from in-MOF for enhanced photocatalytic hydrogen evolution. *ACS Catal.* **2021**, *11*, 6276–6289.
[115] Wang, Y. N.; Guo, L. N.; Zeng, Y. Q.; Guo, H. W.; Wan, S. P.; Ou, M.; Zhang, S. L.; Zhong, Q. Amino-assisted NH_2–UiO-66 anchored on porous g-C_3N_4 for enhanced visible-light-driven CO_2 reduction. *ACS Appl. Mater. Interfaces* **2019**, *11*, 30673–30681.
[116] Ma, R.; Wang, T. Y.; Qian, B. Y.; Xia, Z. Q.; Chen, S. R.; Shi, W. L.; Yang, Q.; Xie, G.; Chen, S. P. Ultrathin Hf-MOF with dinitrogen chelating sites stabilizing and inducing generation of single-rod $Cs_3Bi_2Br_9$ nanocrystals for efficient photocatalytic CO_2 reduction. *J. Am. Chem. Soc.* **2025**, *147*, 32625–32639.
[117] Li, H. Y.; Zhang, J. J.; Zhu, B. C.; He, B. W.; Bie, C. B.; Yu, J. G.; Zhang, L. Y. Orchestrating Ti–S and Ni–S bonding interfaces for accelerated charge transfer in a S-scheme photocatalyst. *Adv. Funct. Mater.* **2026**, *36*, e21318.
[118] Wang, X. H.; Wang, X. H.; Huang, J. F.; Li, S. X.; Meng, A. L.; Li, Z. J. Interfacial chemical bond and internal electric field modulated Z-scheme S_v-$ZnIn_2S_4$/$MoSe_2$ photocatalyst for efficient hydrogen

evolution. *Nat. Commun.* **2021**, *12*, 4112.
[119] Zhu, X. D.; Song, Z. M.; Wang, Z. Y.; Liu, W.; Hong, B.; Bao, J.; Gao, C.; Sun, S. Selective formation of interfacial bonding enables superior hydrogen production in organic-inorganic hybrid cocatalyzed photocatalysts. *Appl. Catal. B: Environ.* **2020**, *274*, 119010.
[120] Wang, K. W.; Hu, Z. F.; Yu, P. F.; Balu, A. M.; Li, K.; Li, L. F.; Zeng, L. Y.; Zhang, C.; Luque, R.; Yan, K. et al. Understanding bridging sites and accelerating quantum efficiency for photocatalytic CO_2 reduction. *Nano-Micro Lett.* **2024**, *16*, 5.
[121] Tu, H.; Tian, B. H.; Chen, S. S.; Xu, J. Y.; Yang, J. R.; Zhao, Z. C.; Chen, S. H.; Wu, J. Enhancing photocatalytic efficiency through surface modification to manipulate internal electron-hole distribution. *npj Clean Water* **2025**, *8*, 48.
[122] Li, Z.; Zhang, Z. H.; Hu, H. S.; Liu, Q. D.; Wang, X. Synthesis of two-dimensional polyoxoniobate-based clusterphenes with in-plane electron delocalization. *Nat. Synth.* **2023**, *2*, 989–997.
[123] Zou, S. R.; Liu, Y.; Huang, G. M.; Ding, X.; Zhou, X.; Xiong, M. H.; Shan, Y. W.; Jiang, B.; Chen, H.; Wang, S. Y. High-throughput electron transfer in inorganic-organic interfacial electric field enabling selective CO_2 photoreduction. *Angew. Chem., Int. Ed.* **2025**, *64*, e202516801.
[124] Qi, Y. Y.; Sun, H.; She, P.; Wu, J. H.; Han, J. W.; Xu, Q.; Qin, J. S.; Rao, H. Dithiocarbamate-linked phthalocyanine with CdSe QDs enhancing charge transfer for selective photocatalytic CO_2 reduction. *Adv. Funct. Mater.* **2025**, *35*, 2505021.
[125] Dong, J. R.; Yang, Z. J.; Li, H.; Li, Y. W.; Wei, J. J. Boosting CO_2 photoreduction through dispersing quantum dots in viscous polymer networks. *J. Am. Chem. Soc.* **2025**, *147*, 39599–39609.
[126] Cai, Z. J.; Liu, H. W.; Dai, J. J.; Li, B.; Yang, L. M.; Wang, J. Y.; Zhu, H. Y. Sunlight-driven simultaneous CO_2 reduction and water oxidation using indium-organic framework heterostructures. *Nat. Commun.* **2025**, *16*, 2601.
[127] Du, C. Y.; Sheng, J. P.; Zhong, F. Y.; He, Y.; Liu, H. Y.; Sun, Y. J.; Dong, F. Boosting exciton dissociation and charge transfer in $CsPbBr_3$ QDs via ferrocene derivative ligation for CO_2 photoreduction. *Proc. Natl. Acad. Sci. USA* **2024**, *121*, e2315956121.
[128] Gui, W. K.; Jiang, S.; Wang, L. Y.; Liu, C. W.; Huang, Z. C.; Wang, L.; Yang, J. P. Construction of asymmetric anion layer to accelerate carrier reaction kinetics and thermodynamically promote photocatalytic CO_2 reduction. *Adv. Funct. Mater.* **2025**, *35*, 2505919.
[129] Peng, H. P.; Yang, T.; Lin, H. P.; Xu, Y.; Wang, Z. H.; Zhang, Q. H.; Liu, S. H.; Geng, H. B.; Gu, L.; Wang, C. et al. Ru/In dual-single atoms modulated charge separation for significantly accelerated photocatalytic H_2 evolution in pure water. *Adv. Energy Mater.* **2022**, *12*, 2201688.
[130] Zhu, A. N.; Cao, Y. T.; Zhao, N.; Jin, Y. C.; Li, Y. L.; Yang, L.; Zhang, C. C.; Gao, Y. X.; Zhang, Z.; Zhang, Y. Y. et al. Geminal synergy in Pt–Co dual-atom catalysts: From synthesis to photocatalytic hydrogen production. *J. Am. Chem. Soc* **2024**, *146*, 33002–33011.
[131] Li, B.; Zheng, H. S.; Zhou, T.; Lu, Q. J.; Chen, M. P.; Sun, H. C.; Zhang, Y. X.; Zhang, Y. M.; Li, D. Q.; Zi, B. Y. et al. Asymmetric coordination enhances the synergy of Pt species dual active sites for efficient photocatalytic H_2 evolution. *Nat. Commun.* **2025**, *16*, 8276.
[132] Holmes-Gentle, I.; Tembhurne, S.; Suter, C.; Haussener, S. Kilowatt-scale solar hydrogen production system using a concentrated integrated photoelectrochemical device. *Nat. Energy* **2023**, *8*, 586–596.
[133] Zhan, X. H.; Weng, Z. W.; Ren, D. D.; Tong, X. F.; Liu, J. Y.; Gao, R.; Shi, H. X. Dual-atom catalysts beyond single-atom limitations: Mn/Co synergistic sites on crystalline g-C_3N_4 boosting photocatalysis. *J. Alloys Compd.* **2025**, *1030*, 180874.
[134] Yu, Z. P.; Li, Y. F.; Torres-Pinto, A.; LaGrow, A. P.; Diaconescu, V. M.; Simonelli, L.; Sampaio, M. J.; Bondarchuk, O.; Amorim, I.; Araujo, A. et al. Single-atom Ir and Ru anchored on graphitic carbon nitride for efficient and stable electrocatalytic/photocatalytic hydrogen evolution. *Appl. Catal. B: Environ.* **2022**, *310*, 121318.
[135] Zhou, M.; Wang, Z. Q.; Mei, A. H.; Yang, Z. F.; Chen, W.; Ou, S. Y.; Wang, S. Y.; Chen, K. Q.; Reiss, P.; Qi, K. et al. Photocatalytic CO_2 reduction using La–Ni bimetallic sites within a covalent organic framework. *Nat. Commun.* **2023**, *14*, 2473.
[136] Li, J.; Huang, H. L.; Xue, W. J.; Sun, K.; Song, X. H.; Wu, C. R.; Nie, L.; Li, Y.; Liu, C. Y.; Pan, Y. et al. Self-adaptive dual-metal-site pairs in metal-organic frameworks for selective CO_2 photoreduction to CH_4. *Nat. Catal.* **2021**, *4*, 719–729.
[137] Wang, G.; Chen, Z.; Wang, T.; Wang, D. S.; Mao, J. J. P and Cu dual sites on graphitic carbon nitride for photocatalytic CO_2 reduction to hydrocarbon fuels with high C_2H_6 evolution. *Angew. Chem., Int. Ed.* **2022**, *61*, e202210789.
[138] Yan, G. C.; Xu, B. R.; Zhang, R. Y.; Teng, W. K.; Zhou, T.; Li, H.; Hua, W. B.; Lin, B.; Yang, G. D. Noble-metal-free Ni–W dual-atom sites with bifunctional synergy for efficient photocatalytic CO_2 conversion. *Appl. Catal. B: Environ. Energy* **2025**, *378*, 125535.
[139] Deng, A. X.; Zhao, E.; Li, Q.; Sun, Y.; Liu, Y. Z.; Yang, S. G.; He, H.; Xu, Y.; Zhao, W.; Song, H. O. et al. Atomic cobalt-silver dual-metal sites confined on carbon nitride with synergistic Ag nanoparticles for enhanced CO_2 photoreduction. *ACS Nano* **2023**, *17*, 11869–11881.
[140] Hu, B.; Li, Z. Y.; Wang, B. H.; Chen, L.; Wang, X.; Hu, X. S.; Bai, Z. J.; Li, Y.; Chen, G. H.; Luo, X. et al. Construction of Co–In dual single-atom catalysts for photocatalytic CO_2 reduction into CH_4. *Appl. Catal. B: Environ. Energy* **2025**, *371*, 125196.
[141] Liu, B.; Cheng, M.; Zhang, C. Y.; Si, Y. T.; Zhou, J. C.; Ren, Y. Q.; Guan, J.; Duan, L. B.; Liu, M. C.; Jing, D. W. et al. Au–Cu dual-single-atom sites on Bi_2WO_6 with oxygen vacancy for CO_2 photoreduction towards multicarbon products. *Appl. Catal. B: Environ. Energy* **2024**, *357*, 124263.
[142] Song, W. T.; Song, B.; Liang, Y. H.; Zhou, Y.; Wang, B.; Gao, W. G.; Wu, Y.; Ling, X.; Liu, Y.; Ye, R. Q. et al. Precise dual-metal pairs enable ultrafast structural response for CO_2-to-ethylene photoconversion. *J. Am. Chem. Soc.* **2025**, *147*, 39505–39515.
[143] Zhang, W. J.; Hao, X. W.; Liu, X. L.; Chu, M. Y.; Li, S. M.; Wang, X. C.; Jiang, F.; Wang, L.; Zhang, Q.; Chen, J. X. et al. Photocatalytic conversion of polyester-derived alcohol into value-added chemicals by engineering atomically dispersed Pd catalyst. *Angew. Chem., Int. Ed.* **2025**, *64*, e202500814.
[144] Chu, M. Y.; Tu, W. L.; Zhuang, Z. C.; Xu, P. P.; Weng, X. F.; Wang, J. H.; Yan, T. R.; Zhang, L.; Cao, M. H.; Zhang, L. et al. Efficient polyolefin upcycling over single-atom alloy catalyst. *CCS Chem.* **2025**, *7*, 2451–2464.
[145] Liu, Y.; Wang, X. C.; Li, X. D.; Ye, Z. Y.; Sham, T. K.; Xu, P. P.; Cao, M. H.; Zhang, Q.; Yin, Y. D.; Chen, J. X. Universal and scalable synthesis of photochromic single-atom catalysts for plastic recycling. *Nat. Commun.* **2024**, *15*, 9357.
[146] Zhu, Z. J.; Hu, J. C.; Hu, C.; Lu, Y.; Chu, S. Q.; Chen, F.; Zhang, Y. H.; Huang, H. W. Oriented crystal polarization tuning bulk charge and single-site chemical state for exceptional hydrogen photo-production. *Adv. Mater.* **2024**, *36*, 2411339.
[147] Wang, Z. N.; Zhou, D. Y. Y.; Tian, K. G.; Chen, G. L.; Li, Y. Y.; Liu, S. F.; Lee, S. T.; Ji, Y. J.; Yan, J. Q. Dipole synergy enables fast directional charge transport for solar hydrogen and benzaldehyde coproduction. *Nat. Commun.* **2025**, *16*, 11066.
[148] Wan, S. J.; Wang, W.; Cheng, B.; Luo, G. Q.; Shen, Q.; Yu, J. G.; Zhang, J. J.; Cao, S. W.; Zhang, L. M. A superlattice interface and S-scheme heterojunction for ultrafast charge separation and transfer in photocatalytic H_2 evolution. *Nat. Commun.* **2024**, *15*, 9612.
[149] Liu, M. C.; Jing, D. W.; Zhou, Z. H.; Guo, L. J. Twin-induced one-dimensional homojunctions yield high quantum efficiency for solar hydrogen generation. *Nat. Commun.* **2013**, *4*, 2278.
[150] Yang, D. R.; Zuo, S. W.; Yang, H. Z.; Wang, X. Single-unit-cell catalysis of CO_2 electroreduction over sub-1 nm Cu_9S_5 nanowires.

Adv. Energy Mater. **2021**, *11*, 2100272.
[151] Wang, X.; Liu, B. Y.; Ma, S. Q.; Zhang, Y. J.; Wang, L. Z.; Zhu, G. Q.; Huang, W.; Wang, S. C. Induced dipole moments in amorphous ZnCdS catalysts facilitate photocatalytic H_2 evolution. *Nat. Commun.* **2024**, *15*, 2600.
[152] Yuan, Q. C.; Liu, D.; Zhang, N.; Ye, W.; Ju, H. X.; Shi, L.; Long, R.; Zhu, J. F.; Xiong, Y. J. Noble-metal-free Janus-like structures by cation exchange for Z-scheme photocatalytic water splitting under broadband light irradiation. *Angew. Chem., Int. Ed.* **2017**, *56*, 4206–4210.
[153] Zhang, Q.; Chen, J. X.; Xie, Y. Y.; Wang, M. Z.; Ge, X. W. Inductive effect of poly(vinyl pyrrolidone) on morphology and photocatalytic performance of Bi_2WO_6. *Appl. Surf. Sci.* **2016**, *368*, 332–340.
[154] Chen, J. X.; Jiang, F.; Yin, Y. D. Manipulation of interfacial diffusion for controlling nanoscale transformation. *Acc. Chem. Res.* **2021**, *54*, 1168–1177.

Haiqing Wang is a professor at the Institute of Advanced Interdisciplinary Research (IAIR), University of Jinan. He serves as a council member of the Tsinghua Chemistry Alumni Association and is listed among the "World's Top 2% Scientists". His research focuses on the controllable synthesis and precise regulation of cluster assemblies, nanostructures, and interfaces, with an emphasis on photo-thermal-electrical coupling for efficient CO_2 reduction and conversion. He has published over 40 SCI papers in CAS Q1 journals as first or corresponding author and has received funding from the NSFC and Shandong Province.